LETTERS
https://doi.org/10.1038/s41591-020-01143-2

nature medicine

Check for updates

Characterization of pre-existing and induced SARS-CoV-2-specific CD8+ T cells

Isabel Schulien[1,17], Janine Kemming[1,2,17], Valerie Oberhardt[1,2,17], Katharina Wild[1,3,17], Lea M. Seidel[1,2,4,5,17], Saskia Killmer[1,17], Sagar[6], Franziska Daul[1,2], Marilyn Salvat Lago[1], Annegrit Decker[1], Hendrik Luxenburger[1,7], Benedikt Binder[1,7], Dominik Bettinger[1,8], Oezlem Sogukpinar[1], Siegbert Rieg[1], Marcus Panning[9], Daniela Huzly[9], Martin Schwemmle[9], Georg Kochs[9], Cornelius F. Waller[10], Alexandra Nieters[11], Daniel Duerschmied[12], Florian Emmerich[13], Henrik E. Mei[14], Axel Ronald Schulz[14], Sian Llewellyn-Lacey[15], David A. Price[15,16], Tobias Boettler[1,8,18], Bertram Bengsch[1,5,18], Robert Thimme[1,18] ✉, Maike Hofmann[1,18] ✉ and Christoph Neumann-Haefelin[1,18] ✉

Emerging data indicate that SARS-CoV-2-specific CD8+ T cells targeting different viral proteins are detectable in up to 70% of convalescent individuals[1–5]. However, very little information is currently available about the abundance, phenotype, functional capacity and fate of pre-existing and induced SARS-CoV-2-specific CD8+ T cell responses during the natural course of SARS-CoV-2 infection. Here, we define a set of optimal and dominant SARS-CoV-2-specific CD8+ T cell epitopes. We also perform a high-resolution ex vivo analysis of pre-existing and induced SARS-CoV-2-specific CD8+ T cells, applying peptide-loaded major histocompatibility complex class I (pMHCI) tetramer technology. We observe rapid induction, prolonged contraction and emergence of heterogeneous and functionally competent cross-reactive and induced memory CD8+ T cell responses in cross-sectionally analyzed individuals with mild disease following SARS-CoV-2 infection and three individuals longitudinally assessed for their T cells pre- and post-SARS-CoV-2 infection. SARS-CoV-2-specific memory CD8+ T cells exhibited functional characteristics comparable to influenza-specific CD8+ T cells and were detectable in SARS-CoV-2 convalescent individuals who were seronegative for anti-SARS-CoV-2 antibodies targeting spike (S) and nucleoprotein (N). These results define cross-reactive and induced SARS-CoV-2-specific CD8+ T cell responses as potentially important determinants of immune protection in mild SARS-CoV-2 infection.

We selected five in silico predicted, SARS-CoV-2-derived epitope candidate peptides for each of the following human leukocyte antigen (HLA) class I alleles that are common in most populations worldwide (Extended Data Fig. 1): A*01:01, A*02:01, A*03:01, A*11:01 and A*24:02, as well as B*07:02, B*08:01, B*15:01, and B*40:01 and eight epitope candidate peptides for B*44:02/03 (Supplementary Table 1). In addition, we included all 13 previously described SARS-CoV-1-specific CD8+ T cell epitopes that display 100% homology in SARS-CoV-2[6] (Supplementary Table 1). We tested these 66 epitope peptides in 26 individuals (of white ancestry) with convalescent mild SARS-CoV-2 infection (Supplementary Table 2) in HLA-matched peptide-specific cell cultures. Importantly, we could detect SARS-CoV-2-specific CD8+ T cell responses in 23 out of 26 (88.5%) individuals, targeting a median of four epitopes (range 1–12; Fig. 1a). This exceeds the previously reported high detection rate of T cell responses in up to 70% of convalescent individuals in different cohorts using peptide pools for T cell stimulation[1–5], probably reflecting our non-competitive approach. Identified CD8+ T cell epitopes were restricted by both HLA types, HLA-A and HLA-B (Fig. 1b). Thirty-three of 53 (62.3%) SARS-CoV-2-specific epitope candidates predicted in our study could be confirmed (Supplementary Table 1, depicted in bold). The strongest responses were observed for epitopes A*01/ORF3a$_{207–215}$, A*02/ORF3a$_{139–147}$ and B*07/N$_{105–113}$, with medians of 8.3, 8.4 and 62.6% of CD8+ T cells producing interferon (IFN)-γ after peptide-specific culture,

[1]Department of Medicine II (Gastroenterology, Hepatology, Endocrinology and Infectious Diseases), Freiburg University Medical Center, Faculty of Medicine, University of Freiburg, Freiburg, Germany. [2]Faculty of Biology, University of Freiburg, Freiburg, Germany. [3]Faculty of Chemistry and Pharmacy, University of Freiburg, Freiburg, Germany. [4]SGBM – Spemann Graduate School of Biology and Medicine, University of Freiburg, Freiburg, Germany. [5]Signalling Research Centres BIOSS and CIBSS, University of Freiburg, Freiburg, Germany. [6]Max Planck Institute of Immunobiology and Epigenetics, Freiburg, Germany. [7]IMM-PACT, Faculty of Medicine, University of Freiburg, Freiburg, Germany. [8]Berta-Ottenstein Programme, Faculty of Medicine, University of Freiburg, Freiburg, Germany. [9]Institute of Virology, Freiburg University Medical Center, Faculty of Medicine, University of Freiburg, Freiburg, Germany. [10]Department of Haematology, Oncology & Stem Cell Transplantation, Freiburg University Medical Center, Faculty of Medicine, University of Freiburg, Freiburg, Germany. [11]Center for Biobanking–FREEZE-Biobanking, Freiburg University Medical Center, Faculty of Medicine, University of Freiburg, Freiburg, Germany. [12]Department of Medicine III (Interdisciplinary Medical Intensive Care), Freiburg University Medical Center, Faculty of Medicine, University of Freiburg, Freiburg, Germany. [13]Institute for Transfusion Medicine and Gene Therapy, Freiburg University Medical Center, Faculty of Medicine, University of Freiburg, Freiburg, Germany. [14]German Rheumatism Research Center Berlin (DRFZ), Berlin, Germany. [15]Division of Infection and Immunity, Cardiff University School of Medicine, Cardiff, UK. [16]Systems Immunity Research Institute, Cardiff University School of Medicine, Cardiff, UK. [17]These authors contributed equally: Isabel Schulien, Janine Kemming, Valerie Oberhardt, Katharina Wild, Lea M. Seidel, Saskia Killmer. [18]These authors jointly supervised this work: Tobias Boettler, Bertram Bengsch, Robert Thimme, Maike Hofmann, Christoph Neumann-Haefelin. ✉e-mail: robert.thimme@uniklinik-freiburg.de; maike.hofmann@uniklinik-freiburg.de; christoph.neumann-haefelin@uniklinik-freiburg.de

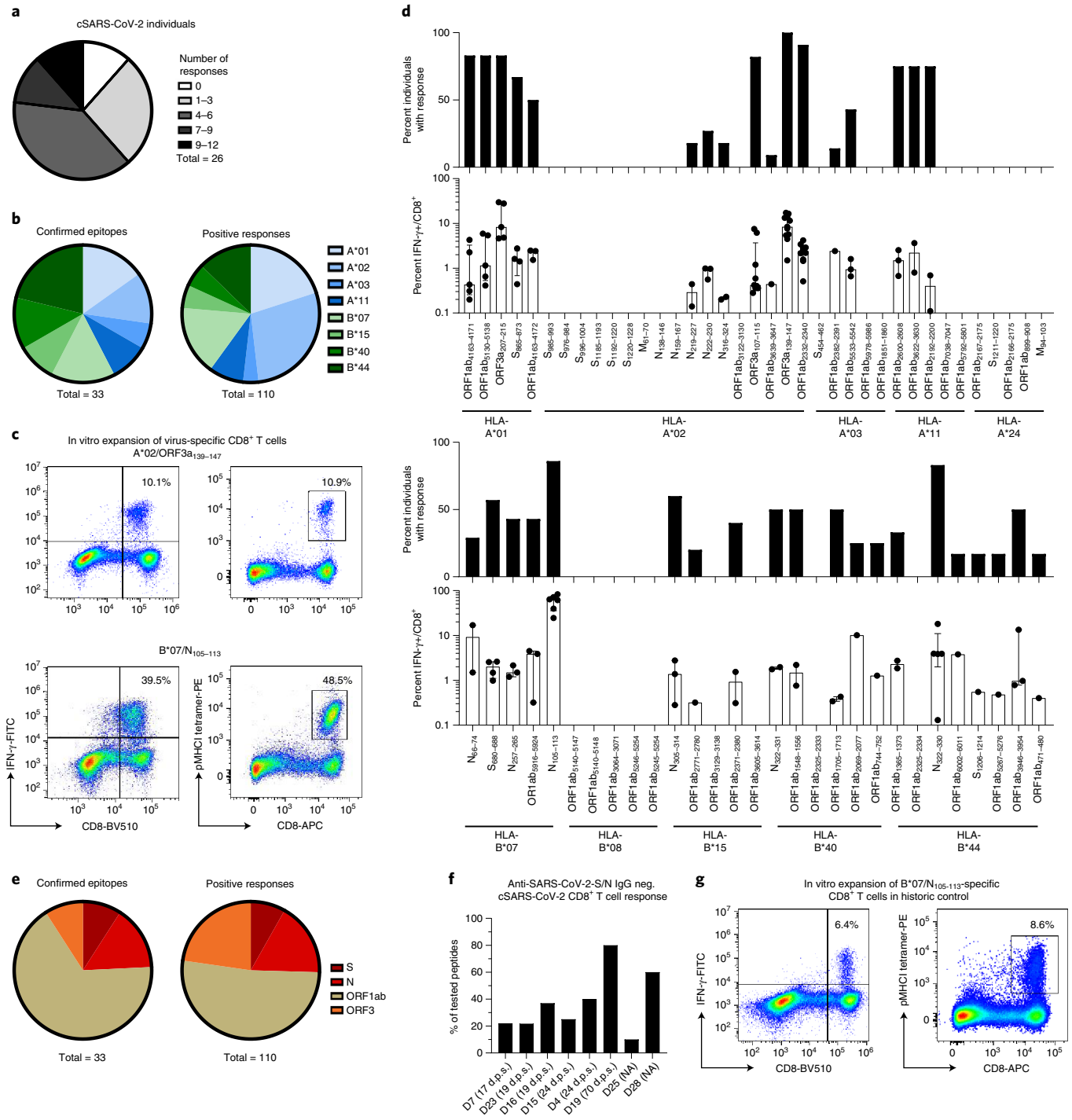

Fig. 1 | Dominant SARS-CoV-2-specific CD8⁺ T cell epitopes. a, Pie chart illustrating the number of epitopes recognized per tested individual. **b**, Confirmed epitopes and total positive responses, depicted according to their HLA restriction. **c**, Representative dot plots showing peptide-loaded major histocompatibility complex class I (pMHCI) tetramer stainings and IFN-γ production of A*02/ORF3a$_{139–147}$- and B*07/N$_{105–113}$-specific CD8⁺ T cells after 14 days of in vitro expansion. Numbers refer to the respective percentage of pMHCI-tetramer⁺ and IFN-γ⁺ cells among CD8⁺ T cells. **d**, Percentage of convalescent SARS-CoV-2 individuals with a positive response toward HLA-A- and HLA-B-restricted SARS-CoV-2 peptides and the strength of individual responses as percent IFN-γ⁺ of CD8⁺ T cells. **e**, Confirmed epitopes and total positive responses depicted according to their location within the SARS-CoV-2 genome. **f**, CD8⁺ T cell responses in anti-SARS-CoV-2 S IgG (EUROIMMUN test, detection limit: 1.2 a.u. ml^{-1}) and anti-SARS-CoV-2 N IgG (Mikrogen test, detection limit: 24 a.u. ml^{-1}) seronegative convalescent individuals as percentage of responses out of all peptides tested matching the patient's HLA alleles. Days post symptom onset (d.p.s.) are indicated. **g**, Exemplary dot plots showing pMHCI-tetramer staining and IFN-γ production of HLA-B*07/N$_{105–113}$-specific CD8⁺ T cells from a historic control after 14 days in vitro expansion. Numbers refer to the respective percentage of pMHCI-tetramer⁺ and IFN-γ⁺ cells among CD8⁺ T cells. Bar charts show the median with interquartile range (IQR). $n = 26$ convalescent individuals. NA, not applicable (asymptomatic).

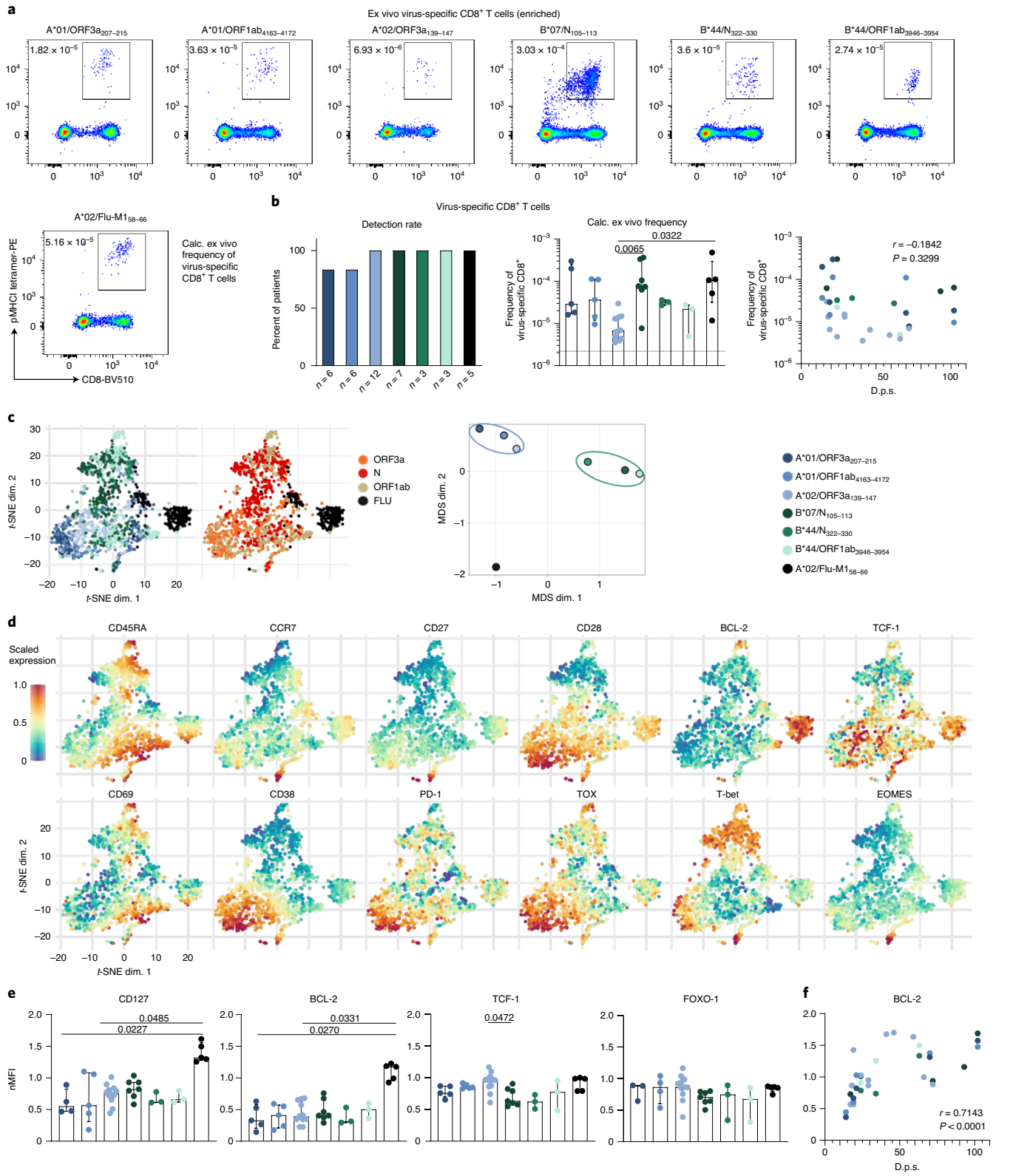

Fig. 2 | Ex vivo phenotypes of SARS-CoV-2-specific CD8⁺ T cells. a, Epitope-specific CD8⁺ T cells ex vivo after pMHCI tetramer-based enrichment (10 to 20×10^6 peripheral blood mononuclear cells, PBMCs). Calculated ex vivo frequencies are depicted. **b**, Detection rates (left) and frequencies (middle) of epitope-specific T cells and their correlation with d.p.s. (right). **c**, *t*-SNE representation of fluorescence-activated cell sorting (FACS) data comparing T cells by HLA restriction (left) and targeted viral proteins (middle). MDS analysis results are also shown comparing HLA-A- and HLA-B-restricted epitopes (right). **d**, Expression levels (blue, low; red, high) of the indicated markers plotted on *t*-SNE plots. **e**, median fluorescence intensity (MFI) of indicated markers on virus-specific T cells normalized to MFI of naive T cells (nMFI). **f**, Correlation of BCL-2 expression with d.p.s. Bar charts show median with IQR. $n = 6$ (A*01/ORF3a$_{207–215}$, A*01/ORF1ab$_{4163–4172}$), $n = 12$ (A*02/ORF3a$_{139–147}$), $n = 7$ (B*07/N$_{105–113}$), $n = 3$ (B*44/N$_{322–330}$, B*44/ORF1ab$_{3946–3954}$), $n = 5$ (A*02/Flu-M1$_{58–66}$). Kruskal–Wallis rank-sum tests including Dunn's multiple comparisons and Spearman correlation were performed.

respectively (Fig. 1c,d). Taking the protein length into account, we observed an over-representation of N- and ORF3a-specific CD8+ T cell responses (Fig. 1e). Despite this, the absolute majority of detectable responses (57/110, 51.8%) targeted ORF1ab (Fig. 1e). This finding highlights the broad recognition of SARS-CoV-2 by virus-specific CD8+ T cells shown in earlier work[1]. Our approach to define optimal CD8+ T cell epitopes has the limitation that it does not completely cover the entire viral genome, in contrast to studies that have used overlapping peptides[1,5,7], and therefore does not allow general assessment of immunodominance. Of note, we were able to detect SARS-CoV-2-specific CD8+ T cell responses in eight convalescent individuals that were seronegative for anti-SARS-CoV-2 S and N immunoglobulin-G (IgG) (Fig. 1f). To determine whether the identified SARS-CoV-2-specific CD8+ T cell epitopes are unique to SARS-CoV-2-exposed individuals, we tested historic blood samples (obtained before August 2019) from a cohort of 25 healthy volunteers with gender, age and HLA type characteristics comparable to our SARS-CoV-2 cohort (Supplementary Table 2). We observed very low virus-specific IFN-γ+ and tumor necrosis factor-positive (TNF+) CD8+ T cell responses in six individuals (five individuals, single response; one individual, five responses) (Fig. 1g, Supplementary Table 1 and Extended Data Fig. 2a) and TNF without IFN-γ responses in an additional four individuals (Extended Data Fig. 2a,c). The only epitope that was targeted by IFN-γ-secreting CD8+ T cells in more than one SARS-CoV-2-naive individual was epitope B*07/$N_{105–113}$ (Extended Data Fig. 2a). This is the SARS-CoV-2-specific epitope in our study with the highest conservation between SARS-CoV-2 and 'common cold' coronaviruses (Extended Data Fig. 2b and Supplementary Table 3).

Next, we analyzed ex vivo SARS-CoV-2-specific CD8+ T cells targeting six of the above-identified optimal and dominant epitopes in comparison to influenza (FLU)-specific CD8+ T cells by using a set of peptide-loaded major histocompatibility complex class I (pMHCI) tetramers in a cohort of 20 convalescent individuals following a mild course of infection. Because the ex vivo frequencies of SARS-CoV-2-specific CD8+ T cells turned out to be low (Extended Data Fig. 3a), we performed pMHCI tetramer-based enrichment to increase the detection rate and to allow subsequent in-depth phenotypic analysis (Fig. 2a). After enrichment, we could detect SARS-CoV-2-specific CD8+ T cells in nearly all tested convalescent individuals (Fig. 2b and Extended Data Fig. 3b). SARS-CoV-2-specific CD8+ T cell frequencies were not associated with the time point of analysis during convalescence in relation to onset of symptoms (Fig. 2b and Extended Data Fig. 3c), indicating that the analyzed CD8+ T cell responses were within the late contraction/early memory phase. The calculated ex vivo frequencies of SARS-CoV-2-specific CD8+ T cells targeting A*01/ORF3a$_{207–215}$, A*01/ORF1ab$_{4163–4172}$, A*02/ORF3a$_{139–147}$, B*44:03/$N_{322–330}$ and B*44:03/ORF1ab$_{3946–3954}$ were similar (Fig. 2b). CD8+ T cells targeting B*07/$N_{105–113}$ were present in slightly higher frequencies compared to other SARS-CoV-2-specific CD8+ T cell populations, reaching the levels of A*02/Flu-M1$_{58–66}$-specific CD8+ T cells (Fig. 2b). SARS-CoV-2-specific CD8+ T cell frequencies were generally lower compared to cytomegalovirus (CMV) A*02/pp65$_{496–503}$-specific and Epstein–Barr virus (EBV) A*02/ BMLF1$_{280–288}$-specific CD8+ T cells in the context of latent viral infections associated with 'inflationary memory' CD8+ T cell responses[8], but similar to the frequencies of virus-specific CD8+ T cells (targeting hepatitis B virus (HBV) A*02/pol$_{455–463}$, HBV A*02/core$_{18–27}$ and hepatitis C virus (HCV) A*02/NS3$_{1073–1081}$ and HCV A*02/NS3$_{1406–1415}$) in acutely resolved HBV and HCV infections (Extended Data Fig. 3d). SARS-CoV-2-specific CD8+ T cell populations in convalescent individuals were composed of naive (T_{naive}), central memory (T_{CM}), effector memory 1 (T_{EM1}), effector memory 2 (T_{EM2}), effector memory 3 (T_{EM3}) and terminally differentiated effector memory expressing RA (T_{EMRA}) T cell subsets, irrespective of the targeted epitope (Extended Data Fig. 3e,f). The presence of a minor T_{naive} subset fraction (median, 3.9%) among all tested SARS-CoV-2-specific CD8+ T cells supports the notion that most of these cells have been efficiently primed during the infection. HLA-A- compared to HLA-B-restricted SARS-CoV-2-specific CD8+ T cells showed a shift toward the early differentiated T_{CM} and T_{EM1} subset (Extended Data Fig. 3f). Similar results were obtained by applying the CX_3CR1-based definition of memory T cell subsets (Extended Data Fig. 3g). In addition, *t*-distributed stochastic neighbor embedding (*t*-SNE) and multidimensional scaling (MDS) of all analyzed SARS-CoV-2-specific CD8+ T cells from the tested convalescent individuals (Fig. 2c) separated these cells more clearly according to their HLA restriction compared to the targeted viral protein. HLA-A-restricted SARS-CoV-2-specific CD8+ T cells were characterized by a cluster of markers including CD38, PD-1 and TOX, which are associated with antigen recognition and less differentiated cells expressed CD28 and T cell–specific transcription factor-1 (TCF-1) (Fig. 2d). By contrast, HLA-B-restricted SARS-CoV-2-specific CD8+ T cells clustered based on CD45RA, CD57, KLRG-1, CD25, CX_3CR1 and high T-bet expression probably reflect a more terminally differentiated effector cell state (Fig. 2d and Extended Data Fig. 4a). Of note, FLU-A*02/M1$_{58–66}$-specific CD8+ T cells showed differences compared to HLA-A and HLA-B-restricted SARS-CoV-2-specific CD8+ T cells (Fig. 2c,d). In particular, FLU A*02/M1$_{58–66}$-specific CD8+ T cells expressed higher levels of CD127 and B cell lymphoma-2 (BCL-2), but TCF-1 and Forkhead box protein O1 (FOXO1) were similarly expressed (Fig. 2e and Extended Data Fig. 4b). The reduced BCL-2 expression of SARS-CoV-2-specific CD8+ T cells was most prominent among the early differentiated T_{CM} and T_{EM1} subsets that have the highest BCL-2 expression among memory T cell subsets in general (Extended Data Fig. 4c). BCL-2 expression of SARS-CoV-2-specific CD8+ T cells correlated with time post-onset of symptoms (Fig. 2f). Thus, SARS-CoV-2-specific CD8+ T cells were probably

Fig. 3 | Longitudinal analyses of SARS-CoV-2-specific CD8+ T cell responses. Longitudinal analyses are shown of SARS-CoV-2-infected individual D1. **a**, Timeline showing bleed dates (red arrowheads: light red, early time points; dark red, late time points), symptoms (dark gray bar) and positive PCR testing depicted at d.p.s. The infection time point is indicated with six days prior to symptom onset. **b**, The calculated ex vivo frequencies of B*44/$N_{322–330}$- and B*44/ORF1ab$_{3946–3954}$-specific CD8+ T cells (10 to 20 × 10^6 PBMCs) are indicated versus d.p.s. together with a historic sample. The dashed line indicates the detection threshold. **c**, Anti-SARS-CoV-2 S IgG (black dots; EUROIMMUN test, detection limit: 1.2 a.u. ml^{-1}) and anti-SARS-CoV-2 N IgG (gray squares; Mikrogen test, detection limit: 24 a.u. ml^{-1}) are depicted versus d.p.s. The dashed line indicates the detection limit of both tests. **d**, Diffusion map showing flow cytometry data of B*44/$N_{322–330}$- and B*44/ORF1ab$_{3946–3954}$-specific CD8+ T cells in relation to d.p.s. Protein expression levels are plotted on the diffusion map. **e**, The dynamic expression profile of SARS-CoV-2-specific CD8+ T cells, visualized as a heatmap. Data were collected by mass cytometry. Heatmap coloring represents percent of virus-specific CD8+ T cells expressing a given marker (blue, low expression; red, high expression). **f**, Longitudinal analysis of SARS-CoV-2-infected individual D2. The timeline shows bleed dates, symptoms and positive PCR testing depicted at d.p.s. (left). The frequency of A*02/ORF3a$_{139–147}$-specific T cells (middle) and anti-SARS-CoV-2 S IgG and anti-SARS-CoV-2 N IgG (right) are depicted at d.p.s. together with a historic sample. **g**, Longitudinal analysis of SARS-CoV-2-infected individual D3. The timeline shows bleed dates, symptoms and positive PCR testing depicted at d.p.s. (left). The frequency of A*01/ORF3a$_{207–215}$- and A*01/ORF1ab$_{4163–4172}$-specific T cells (middle) and anti-SARS-CoV-2 S IgG and anti-SARS-CoV-2 N IgG (right) are depicted versus d.p.s. together with a historic sample.

not within a resting state but within the dynamic process of establishing a long-lasting memory compartment.

To better determine the dynamics of the CD8+ T cell response in SARS-CoV-2 infection, we longitudinally analyzed SARS-CoV-2-specific CD8+ T cells in single patients. We had the unique opportunity to longitudinally follow the SARS-CoV-2-specific CD8+ T cell response before, during and after SARS-CoV-2 infection in an HLA-B*44:03+ individual with a defined infection event and documented onset of symptoms (Fig. 3a). B*44:03/$N_{322-330}$- and B*44:03/$ORF1ab_{3946-3954}$-specific CD8+ T cells were clearly expanded as early as seven days post infection (day 1 (d1) after symptom onset; Fig. 3b and Extended Data Fig. 5a). Both T cell populations were not detectable prior to SARS-CoV-2 infection (Fig. 3b and Extended Data Fig. 5a). The kinetics of both T cell responses were similar and the contraction phase lasted at least 70 days, with SARS-CoV-2-specific CD8+ T cells still detectable (frequencies of ~1×10^{-5}) 104 days post symptom onset. The serum anti-SARS-CoV-2 N IgG titer reached the detection limit from day 29 post-symptom onset onward and the anti-SARS-CoV-2 S IgG titer fell below the detection limit at 79 days post symptom onset (Fig. 3c), while

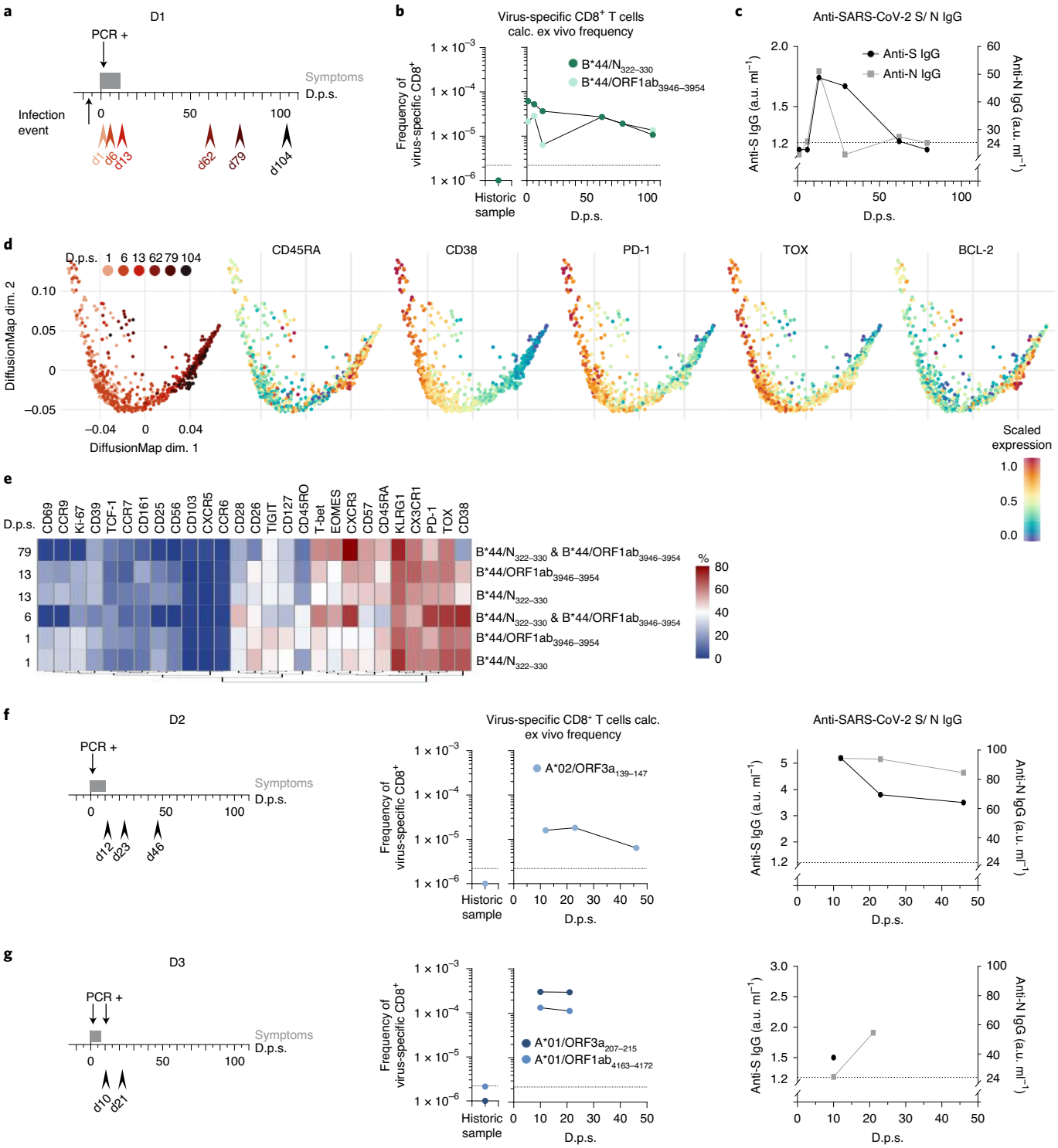

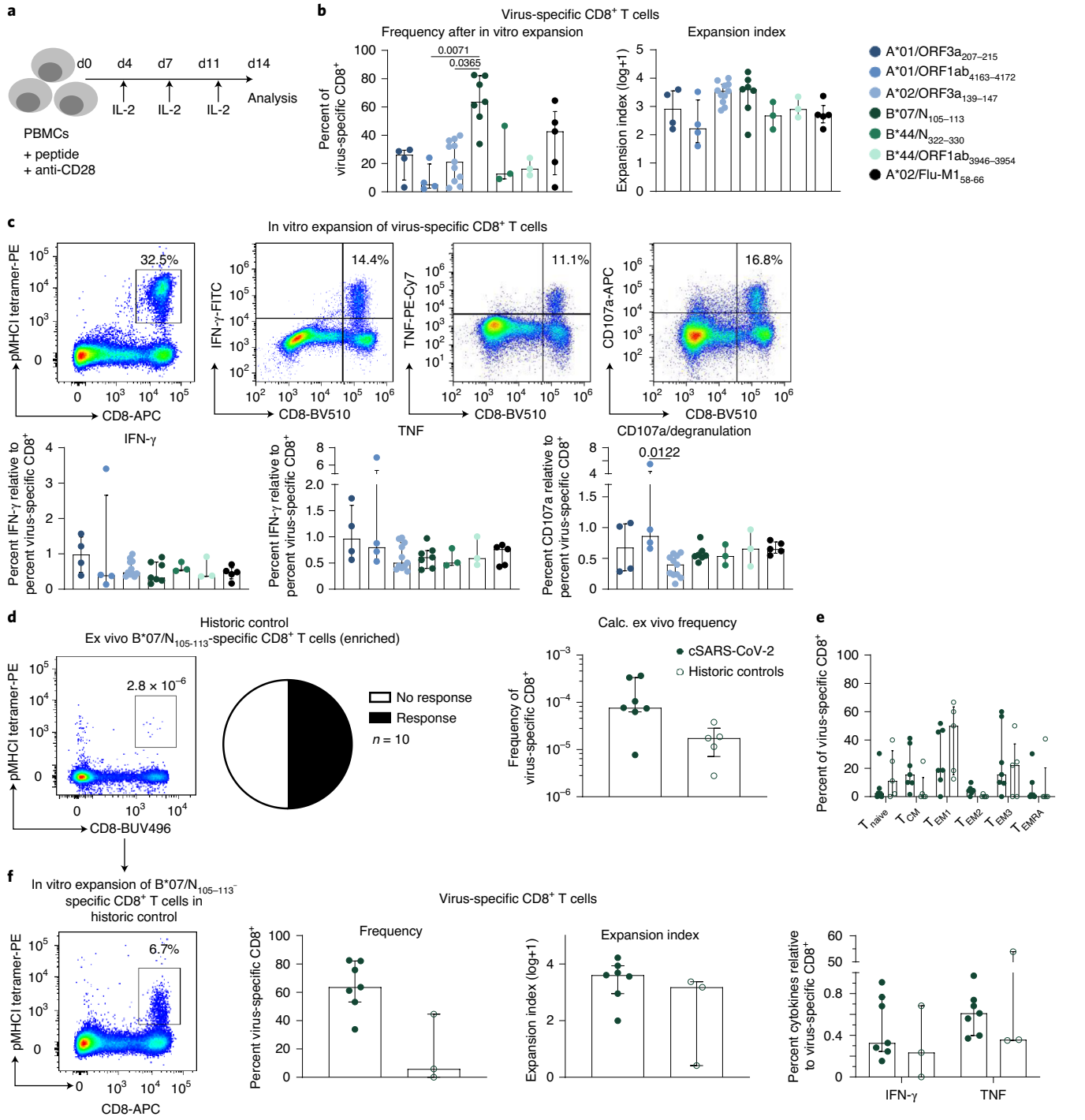

Fig. 4 | Functional capacity of SARS-CoV-2-specific CD8⁺ T cells in vitro. a, Workflow illustrating peptide-specific in vitro expansion of CD8⁺ T cells. **b**, Percentage of virus-specific CD8⁺ T cells (left) and expansion index (right) of the respective epitope-specific CD8⁺ T cells after in vitro expansion. **c**, Dot plots showing SARS-CoV-2-specific CD8⁺ T cells, and IFN-γ-, TNF- and CD107a-producing CD8⁺ T cells after in vitro expansion (top). The percentages of IFN-γ-, TNF- and CD107a-producing CD8⁺ T cells in relation to the frequency of epitope-specific CD8⁺ T cells were determined (bottom). **d**, Left: Dot plot showing virus-specific CD8⁺ T cells ex vivo after B*07/$N_{105-113}$ tetramer-based enrichment (with 10 to 20 × 10^6 PBMCs; left). Calculated ex vivo frequencies of virus-specific CD8⁺ T cells are shown. Right: Pie chart depicting the number of positive responses of patients tested (middle). Frequency of B*07/$N_{105-113}$-specific CD8⁺ T cells in historic controls compared to convalescent SARS-CoV-2 (cSARS-CoV-2) individuals (right). **e**, Distribution of CD8⁺ T cell subsets (T_{naive}, T_{CM}, T_{EM1}, T_{EM2}, T_{EM3} and T_{EMRA}) of B*07/$N_{105-113}$-specific CD8⁺ T cells in historic controls compared to convalescent SARS-CoV-2 individuals. **f**, Left: Dot plot showing virus-specific CD8⁺ T cells after in vitro expansion. The percentage of pMHCI tetramer⁺ cells among CD8⁺ T cells is depicted. Middle: Frequency and expansion index of virus-specific CD8⁺ T cells. Right: Expression of IFN-γ and TNF relative to the frequency of epitope-specific CD8⁺ T cells in historic controls compared to SARS-CoV-2 convalescent individuals. Historic controls were selected for a history of 'common cold' coronavirus infection. The bar charts show the medians with IQR. In **b**,**c**, $n = 6$ (A*01/ORF3a$_{207-215}$, A*01/ORF1ab$_{4163-4172}$), $n = 12$ (A*02/ORF3a$_{139-147}$), $n = 7$ (B*07/$N_{105-113}$), $n = 3$ (B*44/$N_{322-330}$, B*44/ORF1ab$_{3946-3954}$), $n = 5$ (A*02/Flu-M1$_{58-66}$). In **d**–**f**, $n = 7$ (convalescent SARS-CoV-2), $n = 5$ (**d**,**e**) or $n = 3$ (**f**) (historic controls). Statistical significance was assessed by Kruskal–Wallis rank-sum testing including Dunn's multiple comparisons test.

virus-specific CD8+ T cells remained detectable after enrichment at these same time points and also at later follow-up time points. Next, we performed deep profiling of SARS-CoV-2-specific CD8+ T cells, assessing expression of T cell differentiation and activation markers, transcription factors, inhibitory receptors and pro-survival factors with flow and mass cytometry. Diffusion map embedding combining flow cytometry data of B*44:03/$N_{322–330}$- and B*44:03/ORF1ab$_{3946–3954}$-specific CD8+ T cells indicated a continuous relationship between all SARS-CoV-2-specific CD8+ T cells collected during and after infection. Cells from early time points after symptom onset and those from later time points localize at opposing ends in the diffusion map, reflecting a dynamic differentiation of the virus-specific CD8+ T cell response (Fig. 3d and Extended Data Fig. 5b–d). Based on the linearity of the differentiation program suggested by the diffusion map analysis, we performed single-cell trajectory detection using Wanderlust analysis[9] of mass cytometry data to understand the differentiation trajectories in more detail (Extended Data Fig. 6a). This analysis showed that a small fraction of virus-specific T cells identified one week after symptom onset with a CD28+ TCF-1+ CD127+ CD45RA+ phenotype may represent the precursor population of the large pool of effector cells (Extended Data Fig. 6a). As indicated by these Wanderlust (Extended Data Fig. 6a) and diffusion map (Fig. 3d) analyses, phenotyping by accelerated refined community-partitioning (PARC)[10] of mass cytometry data confirmed a significant shift of SARS-CoV-2-specific CD8+ T cells from an early effector state (characterized by CD38, CD39 or PD-1 together with Ki-67) toward a T_{EM} differentiation program (CD45RA, CX_3CR1, KLRG-1, CD57) with little involvement of T_{CM} cells (Fig. 3e and Extended Data Fig. 6b–d). These changes were also apparent on non-pMHCI tetramer+ CD8+ T cells (Extended Data Fig. 6b,e), suggesting broad activation of virus-specific responses targeting other epitopes. This is supported by additional longitudinal analyses of virus-specific CD8+ T cell responses in an HLA-A*02+ individual (up to 45 days post symptom onset, Fig. 3f) and an HLA-A*01+ individual (up to 21 days post symptom onset, Fig. 3g) pre- and post-infection with SARS-CoV-2 also demonstrating vigorous activation of A*02/ORF3a$_{139–147}$-, A*01/ORF3a$_{207–215}$- and A*01/ORF1ab$_{4163–4172}$-specific CD8+ T cells (Fig. 3f,g and Extended Data Fig. 7a). Similar to the B*44:03/$N_{322–330}$- and B*44:03/ORF1ab$_{3946–3954}$-specific CD8+ T cells of the first case, A*02/ORF3a$_{139–147}$-, A*01/ORF3a$_{207–215}$- and A*01/ORF1ab$_{4163–4172}$-specific CD8+ T cells exhibited elevated expression of the activation markers CD69 and CD38 at early time points that decreased over time, while BCL-2, CD127 and CD57 expression increased (Extended Data Fig. 7b). Anti-SARS-CoV-2 S and N IgG were detectable at all analyzed time points during SARS-CoV-2 infection in the last two cases, but these individuals were only followed until day 45 or day 21 post symptom onset, respectively (Fig. 3f,g). Altogether, these data show that SARS-CoV-2-specific CD8+ T cells restricted by different HLA alleles and targeting different epitopes are rapidly activated and expand during SARS-CoV-2 infection.

We then assessed the functional capacity of SARS-CoV-2-specific compared to FLU-specific memory CD8+ T cells in vitro (Fig. 4a). After two weeks of in vitro expansion, we detected comparable frequencies of SARS-CoV-2 B*07/$N_{105–113}$- and FLU A*02/M1$_{58–66}$-specific CD8+ T cells that were higher compared to the other tested SARS-CoV-2-specific CD8+ T cells (Fig. 4b, left). However, when analyzing the expansion index, a measure taking the input number of virus-specific CD8+ T cells into account, we observed comparable in vitro expansion capacities of the analyzed SARS-CoV-2- and FLU-specific CD8+ T cells (Fig. 4b, right). We also analyzed cytokine production (IFN-γ and TNF) and degranulation (CD107a) in relation to the frequency of virus-specific CD8+ T cells after expansion to obtain an approximation for the effector functions of SARS-CoV-2-specific CD8+ T cells. The functional capacity of SARS-CoV-2-specific CD8+ T cells was similar to A*02/Flu-M1$_{58–66}$-specific CD8+ T cells, irrespective of the targeted epitope (Fig. 4c). In the above-described HLA-B*44:03+ individual (Fig. 3a), we did not detect major changes in the in vitro functional capacity of SARS-CoV-2- specific CD8+ T cell populations within a time span of more than 100 days post symptom onset (Extended Data Fig. 8a–c). Together, these findings suggest that SARS-CoV-2-specific CD8+ T cells differentiate into functionally competent bona fide memory T cells comparable to FLU-specific CD8+ T cells, which represent classical, fully functional memory T cells[11].

Finally, we evaluated whether SARS-CoV-2 B*07/$N_{105–113}$-specific memory CD8+ T cell responses differ between SARS-CoV-2 convalescent individuals (collected between 17 and 100 days post symptom onset, Extended Data Fig. 3b) and common cold coronaviruses-exposed individuals. To do this, we analyzed SARS-CoV-2 B*07/$N_{105–113}$-specific CD8+ T cells in historic blood samples of 10 healthy B*07:02+ individuals that had tested positive for anti-common cold coronavirus N IgG (Fig. 4d and Supplementary Table 2). After pMHCI-based enrichment, we detected B*07/$N_{105–113}$-specific CD8+ T cells ex vivo (5 of 10), but at lower frequencies compared to SARS-CoV-2 convalescent individuals (Fig. 4d). The B*07/$N_{105–113}$-specific CD8+ T cell populations analyzed in SARS-CoV-2 convalescent individuals are probably within the late contraction/early memory phase, because no correlation of the frequency with respect to the timing of analysis was detectable (Extended Data Fig. 8d). The CD45RA/CCR7/CD27-based T cell subset distribution revealed a slight shift toward the further differentiated T_{EM3} subset in SARS-CoV-2 convalescent individuals (Fig. 4e). This further differentiation together with the higher ex vivo frequencies of B*07/$N_{105–113}$-specific CD8+ T cells may indicate heterologous stimulation. Still, the B*07/$N_{105–113}$-specific CD8+ T cell frequency was low, especially when comparing to cross-reactive virus-specific CD8+ T cell responses in the context of other viral infections in humans[12]. We did not observe differences in expansion and cytokine production of B*07/$N_{105\ 113}$-specific CD8+ T cell populations in SARS-CoV-2 convalescent individuals compared to historic healthy controls (Fig. 4f).

Altogether, our findings indicate that pre-existing and induced SARS-CoV-2-specific CD8+ T cells represent major determinants of immune protection on an individual as well as population level. Whether our observation that SARS-CoV-2-specific CD8+ T cells were detectable in individuals seronegative for anti-SARS-CoV-2 S or N IgG indicates a faster waning of the antibody response compared to the CD8+ T cell response in SARS-CoV-2 infection, as has been reported for SARS-CoV-1 infection[13,14], needs to be investigated in further detail and in larger cohorts. This requires longitudinal high-resolution analysis of SARS-CoV-2-specific antibodies targeting different viral proteins and of SARS-CoV-2-specific T cells and B cells[15–17]. In this study, we have now established experimental tools for high-resolution ex vivo analyses of SARS-CoV-2-specific CD8+ T cells that will also help to answer the question about the pathogenic versus protective role of virus-specific CD8+ T cells in SARS-CoV-2 infection. In future work, it will be important to evaluate whether differences in pre-existing and induced SARS-CoV-2-specific CD8+ T cell responses are linked to different courses of infection.

Online content

Any methods, additional references, Nature Research reporting summaries, source data, extended data, supplementary information, acknowledgements, peer review information; details of author contributions and competing interests; and statements of data and code availability are available at https://doi.org/10.1038/s41591-020-01143-2.

Received: 4 September 2020; Accepted: 22 October 2020;
Published online: 12 November 2020

References

1. Grifoni, A. et al. Targets of T cell responses to SARS-CoV-2 coronavirus in humans with COVID-19 disease and unexposed individuals. *Cell* **181**, 1489–1501 (2020).
2. Le Bert, N. et al. SARS-CoV-2-specific T cell immunity in cases of COVID-19 and SARS, and uninfected controls. *Nature* **584**, 457–462 (2020).
3. Ni, L. et al. Detection of SARS-CoV-2-specific humoral and cellular immunity in COVID-19 convalescent individuals. *Immunity* **52**, 971–977 (2020).
4. Sekine, T. et al. Robust T cell immunity in convalescent individuals with asymptomatic or mild COVID-19. *Cell* **183**, 158–168 (2020).
5. Peng, Y. et al. Broad and strong memory $CD4^+$ and $CD8^+$ T cells induced by SARS-CoV-2 in UK convalescent individuals following COVID-19. *Nat. Immunol.* **21**, 1336–1345 (2020).
6. Grifoni, A. et al. A sequence homology and bioinformatic approach can predict candidate targets for immune responses to SARS-CoV-2. *Cell Host Microbe* **27**, 671–680 (2020).
7. Weiskopf, D. et al. Phenotype and kinetics of SARS-CoV-2-specific T cells in COVID-19 patients with acute respiratory distress syndrome. *Sci. Immunol.* **5**, eabd2071 (2020).
8. Klenerman, P. The (gradual) rise of memory inflation. *Immunol. Rev.* **283**, 99–112 (2018).
9. Bendall, S. C. et al. Single-cell trajectory detection uncovers progression and regulatory coordination in human B cell development. *Cell* **157**, 714–725 (2014).
10. Stassen, S. V. et al. PARC: ultrafast and accurate clustering of phenotypic data of millions of single cells. *Bioinformatics* **36**, 2778–2786 (2020).
11. van de Sandt, C. E. et al. Human influenza A virus-specific $CD8^+$ T-cell response is long-lived. *J. Infect. Dis.* **212**, 81–85 (2015).
12. Urbani, S. et al. Heterologous T cell immunity in severe hepatitis C virus infection. *J. Exp. Med.* **201**, 675–680 (2005).
13. Cao, W. C., Liu, W., Zhang, P. H., Zhang, F. & Richardus, J. H. Disappearance of antibodies to SARS-associated coronavirus after recovery. *N. Engl. J. Med.* **357**, 1162–1163 (2007).
14. Ng, O. W. et al. Memory T cell responses targeting the SARS coronavirus persist up to 11 years post-infection. *Vaccine* **34**, 2008–2014 (2016).
15. Hachim, A. et al. ORF8 and ORF3b antibodies are accurate serological markers of early and late SARS-CoV-2 infection. *Nat. Immunol.* **21**, 1293–1301 (2020).
16. Liu, L. et al. Potent neutralizing antibodies against multiple epitopes on SARS-CoV-2 spike. *Nature* **584**, 450–456 (2020).
17. Juno, J. A. et al. Humoral and circulating follicular helper T cell responses in recovered patients with COVID-19. *Nat. Med.* **26**, 1428–1434 (2020).

Methods

Study cohort. A total of 26 convalescent individuals (following a mild course of SARS-CoV-2 infection) and 25 age- and sex-matched historic controls (collected before August 2019) of healthy individuals (including pre-infection samples of longitudinal cases) were recruited at the Freiburg University Medical Center, Germany. A mild course of infection was defined as clinical symptoms without signs of respiratory insufficiency. The donor characteristics are summarized in Supplementary Table 2. SARS-CoV-2 infection was confirmed by positive PCR testing from oropharyngeal swab and/or SARS-CoV-2 spike IgG positive antibody testing in the presence of typical symptoms. pMHCI tetramer-based magnetic bead enrichment of virus-specific CD8$^+$ T cells was performed with samples from 18 SARS-CoV-2 convalescent individuals and 10 historic controls. HLA typing was performed by next-generation sequencing and is presented in Supplementary Table 2. Influenza (FLU A*02/M1$_{58-66}$)-specific CD8$^+$ T cell characterization was performed in five SARS-CoV-2 convalescent individuals, CMV (A*02/pp65$_{496-503}$)- and EBV (A*02/BMLF1$_{280-288}$)-specific CD8$^+$ T cells were obtained from 23 healthy individuals and HBV (A*02/pol$_{455-463}$, A*02/core$_{18-27}$)-specific and HCV (A*02/NS3$_{1073-1081}$, A*02/NS3$_{1406-1415}$)-specific CD8$^+$ T cells were analyzed from donors with an acutely resolved HBV ($n=7$) or HCV ($n=5$) infection. Written informed consent was obtained from all participants and the study was conducted according to federal guidelines, local ethics committee regulations (Albert-Ludwigs-Universität, Freiburg, Germany; no. 322/20) and the Declaration of Helsinki (1975).

PBMC isolation. Venous blood samples were collected in ethylenediaminetetraacetic acid-anticoagulated tubes. PBMCs were isolated with lymphocyte separation medium density gradients (Pancoll separation medium, PAN Biotech) and resuspended in RPMI 1640 medium supplemented with 10% FCS, 1% penicillin/streptomycin and 1.5% HEPES buffer 1 mol l^{-1} (complete medium; all additives from Thermo Scientific) and stored at −80 °C until used.

Prediction of SARS-CoV-2-specific CD8$^+$ T cell epitopes. The entire viral amino-acid sequence of SARS-CoV-2 (GenBank: MN908947.3) was analyzed for in silico peptide binding with ANN 4.0 on the Immune Epitope Database website[18]. The five best 8-, 9- or 10-mer peptides calculated for HLA alleles A*01:01, A*02:01, A*03:01, A*11:01, A*24:02, B*07:02, B*08:01, B*15:01, B*40:01 and B*44:02/03 were selected and synthesized for further analysis. Additionally, 13 epitopes that were predicted by Grifoni et al. with high sequence similarity to SARS-CoV-1 were included, as summarized in Supplementary Table 1[6].

Sequence alignment. Sequence homology analyses were performed in Geneious Prime 2020.0.3 (https://www.geneious.com/) using Clustal Omega 1.2.2 alignment with default settings[19]. Reference genomes of human coronaviruses were downloaded from NCBI databases 229E (NC_002645), HKU1 (NC_006577), NL63 (NC_005831), OC43 (NC_006213), MERS (NC_019843) and SARS-CoV-1 (NC_004718). Proteins of human coronaviruses were aligned according to their homology (amino-acid level) only if the protein of interest had a homolog in the respective coronavirus. Confirmed SARS-CoV-2 epitopes were then mapped to the corresponding protein alignment, as summarized in Supplementary Table 3.

Peptides and tetramers. Peptides were synthesized with an unmodified N terminus and an amidated C terminus with standard Fmoc chemistry and a purity of >70% (Genaxxon Bioscience). HLA class I easYmers (immunAware) were loaded with peptide according to the manufacturer's instructions (A*01/ORF3a$_{207-215}$, A*01/ORF1ab$_{4163-4172}$, A*02/ORF3a$_{139-147}$, B*07/N$_{105-113}$) or ordered as peptide-loaded monomers (B*44:03/N$_{322-330}$, B*44:03/ORF1ab$_{3946-3954}$). SARS-CoV-2 peptide-loaded HLA class I tetramers were generated by conjugation of biotinylated peptide-loaded HLA class I easYmers with phycoerythrin (PE)-conjugated streptavidin (Agilent) according to the manufacturer's instructions. Influenza-specific HLA-A*02/M1$_{58-66}$ (GILGFVFTL) tetramers, CMV-specific HLA-A*02/pp65$_{496-503}$ tetramers, EBV-specific HLA-A*02/BMLF1$_{280-288}$ tetramers, HBV-specific HLA-A*02/pol$_{455-463}$ and HLA-A*02/core$_{18-27}$ tetramers and HCV-specific HLA-A*02/NS3$_{1073-1081}$ and HLA-A*02/NS3$_{1406-1415}$ tetramers were generated as described previously[20].

In vitro expansion of virus-specific CD8$^+$ T cells and assessment of effector function. PBMCs ($1-2\times10^6$) were stimulated with epitope-specific peptides (5 µM) and anti-CD28 mAb (0.5 µg ml^{-1}, BD Biosciences) and expanded for 14 days in complete RPMI culture medium containing rIL2 (20 IU ml^{-1}, Miltenyi Biotec). The expansion factor was calculated based on peptide-loaded HLA class I tetramer staining, as described previously[21]. Cytokine production and degranulation were assessed 5 h after re-stimulation with epitope-specific peptides as previously described[21].

Magnetic bead-based enrichment of antigen-specific CD8 T cells. Enrichment of virus-specific CD8$^+$ T cells was performed as described previously[22]. Briefly, 1 to 2×10^7 PBMCs (with an average of 16.5% CD8$^+$ T cells) were labeled for 30 min with PE-coupled peptide-loaded HLA class I tetramers. Subsequent enrichment was performed with anti-phycoerythrin (PE) beads using magnetic-activated cell sorting (MACS) technology (Miltenyi Biotec) according to the manufacturer's protocol. Enriched SARS-CoV-2-specific CD8$^+$ T cells were used for multiparametric flow cytometry analysis. Frequencies of virus-specific CD8$^+$ T cells were calculated as described previously[22], with a detection limit of 2×10^{-6}.

Multiparametric flow cytometry. The following antibodies were used for multiparametric flow cytometry: anti-CCR7-PE-CF594 (cat. no. 150503, dilution 1:50), anti-CCR7-BUV395 (cat. no. 3D12, dilution 1:50), anti-CCR7-BV421 (cat. no. 150503, dilution 1:33), anti-CD4-BV786 (cat. no. L200, dilution 1:200), anti-CD8-BUV496 (cat. no. SK1, dilution 1:100), anti-CD8-BUV510 (cat. no. SK1, dilution 1:100), anti-CD8-APC (cat. no. SK-1, dilution 1:200), anti-CD27-BV605 (cat. no. L128, dilution 1:200), anti-CD28-BV421 (cat. no. CD28.2, dilution 1:100), anti-CD28-BV711 (cat. no. CD28.2, dilution 1:100), anti-CD45RA-BV786 (cat. no. HI100, dilution 1:800), anti-CD45RA-BUV737 (cat. no. HI100, dilution 1:200), anti-CD69-BUV395 (cat. no. FN50, dilution 1:50), anti-CD107a-APC (cat. no. H4A3, dilution 1:100), anti-CD127-BV510 (cat. no. HIL-7R-M21, dilution 1:25), anti-EOMES-PerCP-eF710 (cat. no. WD1928, dilution 1:50), anti-IFN-γ-FITC (cat. no. 25723.11, dilution 1:8), anti-IL-21-PE (cat. no. 3A3-N2.1, dilution 1:25), anti-PD-1-BV786 (cat. no. EH12.1, dilution 1:33) and anti-TNF-PE-Cy7 (cat. no. Mab11, dilution 1:400) (all obtained from BD Biosciences); anti-BCL-2-BV421 (cat. no. 100, dilution 1:200), anti-CD25-BV650 (cat. no. BC96, dilution 1:33), anti-CD38-BV650 (cat. no. HB-7, dilution 1:400), anti-CD57-BV605 (cat. no. QA17A04, dilution 1:100), anti-CX$_3$CR1-APC-eFluor660 (cat. no. 2A9-1, dilution 1:50), anti-CXCR3-PerCP-Cy5.5 (cat. no. G025H7, dilution 1:33), anti-IL-2-PerCP-Cy5.5 (cat. no. MQ1-17H12, dilution 1:100), anti-IL17A-BV605 (cat. no. BL168, dilution 1:100), anti-PD-1-PE-Cy7 (cat. no. EH12.2H7, dilution 1:200), anti-rabbit-PE-CF594 (cat. no. Poly4064, dilution 1:200) and anti-CD45RA-BV510 (cat. no. HI100, dilution 1:200) (all obtained from BioLegend); anti-FOXO-1-pure (cat. no. C29H4, dilution 1:33) and anti-TCF-1-AlexaFluor488 (cat. no. C63D9, dilution 1:100) (Cell Signaling); anti-CD14-APC-eFluor780 (cat. no. 61D3, dilution 1:400), anti-CD19-APC-eFluor780 (cat. no. HIB19, dilution 1:400), anti-CD27-FITC (cat. no. 0323, dilution 1:100), anti-KLRG-1-BV711 (cat. no. 13F12F2, dilution 1:50), anti-T-bet-PE-Cy7 (cat. no. 4B10, dilution 1:200) and anti-TOX-eFluor660 (cat. no. TRX10, dilution 1:100) (eBioscience). A fixable viability dye (eBioscience; APC-eFluor780 dilutions 1:200, 1:400) or ViaProbe (BD Biosciences; cat. no. 7-AAD, dilution 1:33) was used for live/dead discrimination. A FoxP3/transcription factor staining buffer set (eBioscience) and fixation/permeabilization solution kit (BD Biosciences) were used according to the manufacturers' instructions to stain for intranuclear and cytoplasmic molecules, respectively. Fixation of cells in 2% paraformaldehyde (PFA, Sigma) was followed by subsequent analyses on FACSCanto II, LSRFortessa (BD Biosciences) or CytoFLEX (Beckman Coulter) systems. Data analyses were performed with FlowJo 10 (TreeStar).

Dimensionality reduction of multiparametric flow cytometry data. The visualization of multiparametric flow cytometry data was done with R version 4.0.2 using the Bioconductor (release (3.11)) CATALYST package[23]. The analyses were performed on gated virus-specific CD8$^+$ T cells for two panels separately. Analysis of panel 1 (transcription factors) included the markers CD45RA, CCR7, CD27, CD28, BCL-2, TCF-1, CD69, CD38, PD-1, EOMES, T-bet and TOX. Analysis of panel 2 (surface markers) was performed on CCR7, CD45RA, CD27, CD28, CD25, CD127, CD57, KLRG-1, CXCR3, PD-1, CX$_3$CR1 and FOXO-1. Downsampling of cells to the number of cells present in the sample with the fewest cells was performed before dimensionality reduction to facilitate the visualization of different samples. Marker intensities were transformed by arcsinh (inverse hyperbolic sine) with a cofactor of 150. Dimensionality reduction on the transformed data was achieved by *t*-SNE, MDS and diffusion map visualization.

Mass cytometry. Mass cytometry reagents were obtained from Fluidigm or generated by custom conjugation to isotope-loaded polymers using a MAXPAR X8 conjugation kit (Fluidigm). The mass cytometry antibodies used are shown in Supplementary Table 2. Mass cytometry tetramers were generated by tetramerization of pMHCI monomers with streptavidin conjugated to Eu^{151} using a Lightning link conjugation kit (Expedon) Sample barcoding was performed using anti-β2M barcodes, then cells were pooled and staining was performed as previously described[24]. Briefly, the single-cell suspension was pelleted, incubated with 20 µM Lanthanum-139 (Trace Sciences)-loaded maleimido-mono-amine-DOTA (Macrocyclics) in phosphate-buffered saline (PBS) for 10 min at room temperature (RT) for live/dead discrimination. Cells were washed in staining buffer and resuspended in staining buffer containing tetramers, incubated for 30 min at RT and washed twice. Cells were then resuspended in surface antibody cocktail, incubated for 30 min at RT, washed twice in staining buffer, pre-fixed with PFA (Electron Microscopy Sciences) 1.6%, washed, then fixed and permeabilized using FoxP3 staining buffer set (eBioscience) and stained intracellularly for 60 min at RT. Cells were further washed twice before fixation in 1.6% PFA solution containing 125 nM iridium intercalator overnight at 4 °C. Before data acquisition on a CyTOF Helios (Fluidigm), cells were washed twice in PBS and once in cell acquisition solution (CAS; Fluidigm). Mass cytometry data were analyzed after debarcoding and bead-based normalization. For analysis of

mass cytometric data, samples were first gated on iridium intercalator positive, live, single CD45$^+$ CD3$^+$ CD8$^+$ T cells using FlowJo (v10.6). CD8$^+$ T cells were then exported for analysis in Omiq (Omiq). Virus-specific CD8$^+$ T cells were identified by manual gating. A workflow including dimension reduction using optSNE[25], PARC clustering analysis[10] and Wanderlust trajectory analysis[9] was implemented in Omiq. Clustering and dimension reduction analysis were performed based on CD45RA, CD45RO, CCR7, CD28, CD127, CD16, CD25, CD26, CD38, CD39, CD56, CD57, CD69, CD103, CD161, CCR6, CCR9, CXCR3, CXCR5, CXCR6, CX3CR1, CRTH2, TCF-1, TOX, TIGIT, T-bet, EOMES, KLRG-1 and PD-1. Further analysis and heatmap visualization was performed using R (v4.0) (https://www.r-project.org).

Serum IgG determination. SARS-CoV-2-specific antibodies were determined by the EUROIMMUN assay detecting anti-SARS-CoV-2 spike IgG (anti-SARS-CoV-2 S IgG; detection limit, 1.2 a.u. ml^{-1}) and by the Mikrogen assay detecting anti-SARS-CoV-2 nucleocapside IgG (anti-SARS-CoV-2 N IgG; detection limit, 24 a.u. ml^{-1}), as described in the product instructions. Infection with common cold coronaviruses 229E, NL63, OC43 and HKU1 was determined by the Mikrogen recomline assay detecting the anti-nucleocapside IgG of common cold coronaviruses 229E, NL63, OC43 and HKU1 (detection limit defined by the cutoff control provided by the supplier).

Statistics. Statistical analysis was performed with GraphPad Prism 8. Statistical significance was assessed by Kruskal–Wallis testing including Dunn's multiple comparisons test and Spearman correlation ($^*P<0.05$; $^{**}P<0.01$; $^{***}P<0.001$; $^{****}P<0.0001$).

Reporting Summary. Further information on research design is available in the Nature Research Reporting Summary linked to this article.

Data availability

Raw data for this study are provided as the supplementary dataset at https://github.com/sagar161286/SARSCoV2_specific_CD8_Tcells (flow cytometry data) and at https://flowrepository.org/experiments/3159 (mass cytometry data). All requests for additional supporting raw and analyzed data and materials will be reviewed by the corresponding authors to verify if the request is subject to any intellectual property or confidentiality obligations. Patient-related data not included in the paper were generated as part of clinical examination and may be subject to patient confidentiality. Any data and materials that can be shared will be released via a material transfer agreement. Reference viral sequences (SARS-CoV-2 (MN908947.3), 229E (NC_002645), HKU1 (NC_006577), NL63 (NC_005831), OC43 (NC_006213), MERS (NC_019843) and SARS-CoV-1 (NC_004718)) were downloaded from the NCBI database (https://www.ncbi.nlm.nih.gov/). In silico peptide binding was analyzed with ANN 4.0 on the Immune Epitope Database website (https://www.iedb.org/). Source data are provided with this paper.

Code availability

R code to reproduce the analysis of multiparametric flow cytometry data is available at https://github.com/sagar161286/SARSCoV2_specific_CD8_Tcells. Detailed settings for dimension reduction, clustering and trajectory analysis of mass cytometry data is available via the platform Omiq.ai upon request. This request will be reviewed by the corresponding authors to verify if it is subject to any intellectual property or confidentiality obligations.

References

18. Nielsen, M. et al. Reliable prediction of T-cell epitopes using neural networks with novel sequence representations. *Protein Sci.* **12**, 1007–1017 (2003).
19. Sievers, F. et al. Fast, scalable generation of high-quality protein multiple sequence alignments using Clustal Omega. *Mol. Syst. Biol.* **7**, 539 (2011).
20. Price, D. A. et al. Avidity for antigen shapes clonal dominance in CD8$^+$ T cell populations specific for persistent DNA viruses. *J. Exp. Med.* **202**, 1349–1361 (2005).
21. Wieland, D. et al. TCF1$^+$ hepatitis C virus-specific CD8$^+$ T cells are maintained after cessation of chronic antigen stimulation. *Nat. Commun.* **8**, 15050 (2017).
22. Alanio, C., Lemaitre, F., Law, H. K., Hasan, M. & Albert, M. L. Enumeration of human antigen-specific naive CD8$^+$ T cells reveals conserved precursor frequencies. *Blood* **115**, 3718–3725 (2010).
23. Crowell, H., Zanotelli, V., Chevrier, S. & Robinson, M. CATALYST: Cytometry dATa anALYSis Tools. R package version 1.12.2 (2020); https://github.com/HelenaLC/CATALYST
24. Bengsch, B. et al. Epigenomic-guided mass cytometry profiling reveals disease-specific features of exhausted CD8 T cells. *Immunity* **48**, 1029–1045 (2018).
25. Belkina, A. C. et al. Automated optimized parameters for t-distributed stochastic neighbor embedding improve visualization and analysis of large datasets. *Nat. Commun.* **10**, 5415 (2019).

Acknowledgements

We thank all donors for participating in the current study and the FREEZE-Biobank Center for biobanking (Freiburg University Medical Center) and the Medical Faculty for support. The study was funded by the Federal Ministry of Education and Research (grant no. 01KI1722, to G.K., M.H., M.P., M.S. and R.T.) and by a COVID-19 research grant of the Ministry of Science, Research and Art, State of Baden-Wuerttemberg (to C.N.H. and B.B.). The presented work was also supported by CRC/TRR 179-Project 01 and CRC 1160-Project A02 (to R.T.), CRC/TRR 179-Project 02 and CRC 1160-Project A06 (to C.N.H.), CRC/TRR 179-Project 04 (to T.B.), CRC/TRR 179-Project 20 and CRC 1160-Project A02 (to M.H.), CRC/TRR 179-Project 21, CRC 1160-Project A03 and BE-5496/5-1 (to B.B.) of the German Research Foundation (DFG; TRR 179 project no. 272983813; CRC 1160 project no. 256073931). M.H. was supported by a Margarete von Wrangell fellowship (State of Baden-Wuerttemberg). D.B. and T.B. are supported by the Berta-Ottenstein Programme, Faculty of Medicine, University of Freiburg. H.E.M. was supported by DFG ME3644/5-1(project no. 324736178) and D.A.P. by a Wellcome Trust Senior Investigator Award (100326/Z/12/Z). The funding body had no role in the decision to write or submit the manuscript.

Author contributions

I.S., J.K., V.O. and K.W. planned, performed and analyzed experiments with the help of S., F.D. and O.S. L.M.S. and S.K. performed and analyzed mass cytometry data with the assistance of M.S.L. A.D., H.L., B. Binder, D.B., S.R., C.F.W., A.N. and D.D. were responsible for donor recruitment. H.E.M. and A.R.S. provided barcoding reagents for mass cytometry analysis. S.L.-L. and D.A.P. provided influenza $M1_{58}$/A*02 tetramers. F.E. performed four-digit HLA typing by next-generation sequencing. M.P. and D.H. performed antibody testing. M.S. and G.K. provided virological expertise and contributed to data interpretation. B. Bengsch designed and supervised mass cytometry analysis. T.B., R.T., M.H. and C.N.-H. designed the study and contributed to experimental design and planning. I.S., J.K., V.O., R.T., M.H. and C.N.-H. interpreted data and wrote the manuscript. C.N.-H., M.H., R.T., B. Bengsch and T.B. are shared last authors.

Competing interests

The authors declare no competing interests.

Additional information

Extended data is available for this paper at https://doi.org/10.1038/s41591-020-01143-2.

Supplementary information is available for this paper at https://doi.org/10.1038/s41591-020-01143-2.

Correspondence and requests for materials should be addressed to R.T., M.H. or C.N.-H.

Peer review information Saheli Sadanand was the primary editor on this article and managed its editorial process and peer review in collaboration with the rest of the editorial team.

Reprints and permissions information is available at www.nature.com/reprints.

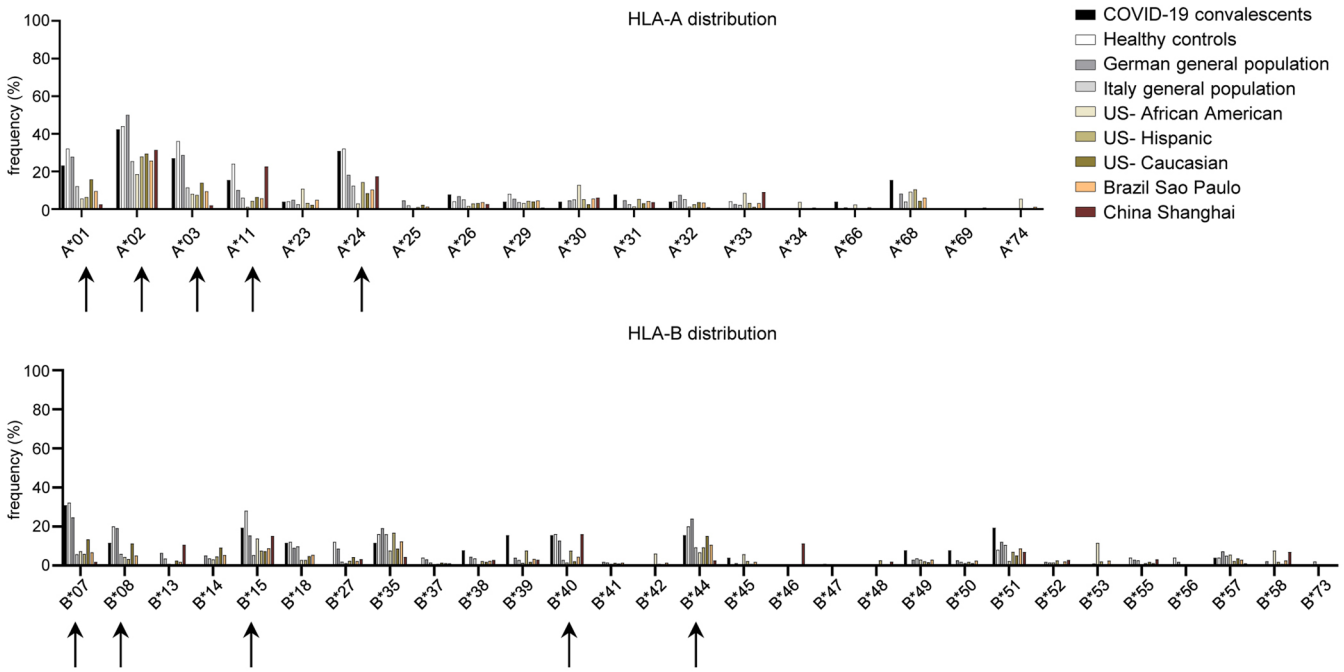

Extended Data Fig. 1 | HLA distribution in different populations. HLA-A and HLA-B distribution in different populations compared to the study population. Arrows indicate HLA alleles for which peptide epitope candidates were predicted and further analyzed.

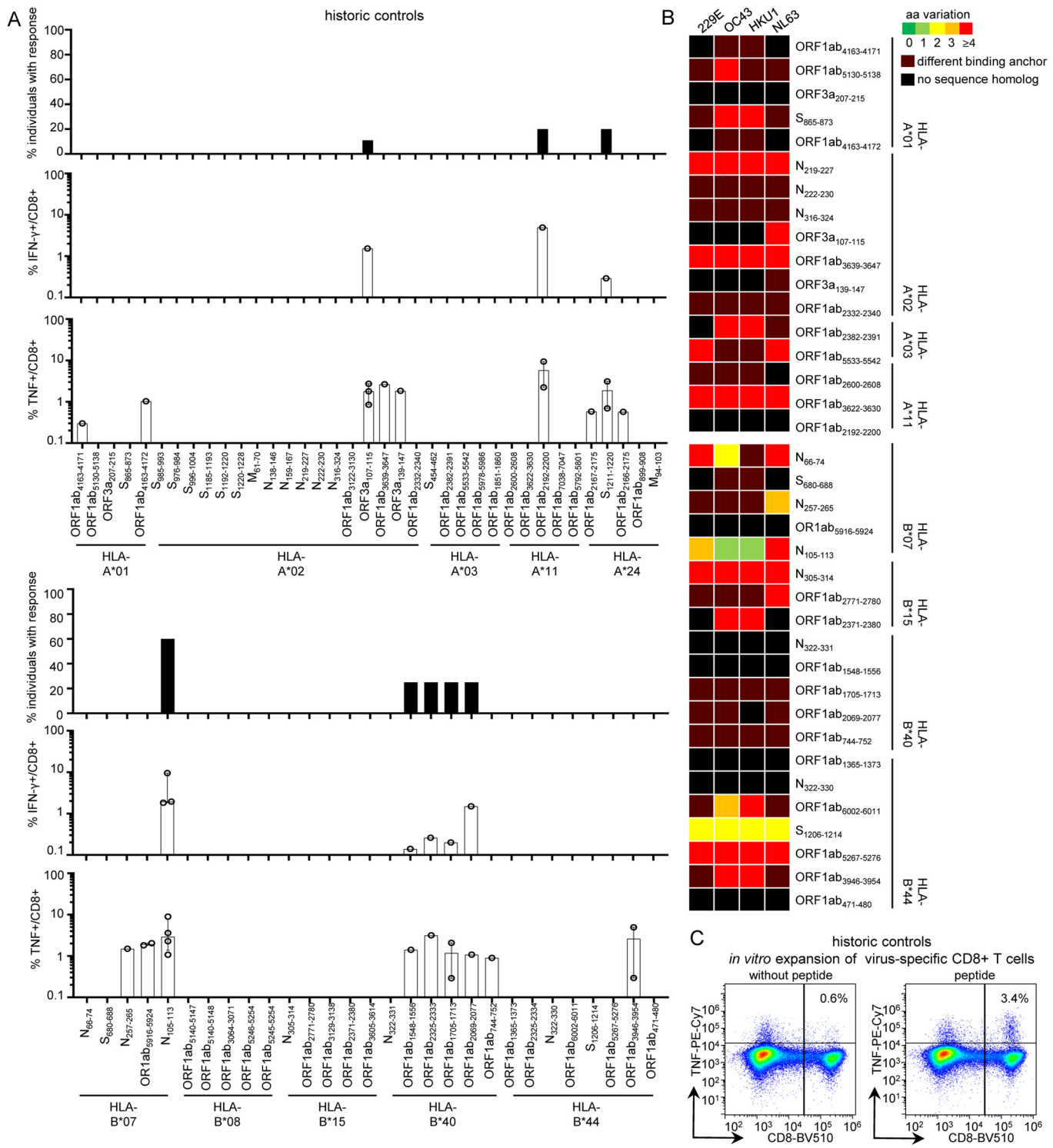

Extended Data Fig. 2 | Cross-reactivity of SARS-CoV-2-specific CD8+ T cells. a, % of historic controls with IFN-γ response towards HLA-A- and HLA-B-restricted SARS-CoV-2 peptides and strength of individual responses as % IFN-γ+ and % TNF+ of CD8+ T cells. **b**, Heat map illustrating the degree of homology between confirmed SARS-CoV-2 epitopes and 'common cold' coronaviruses 229E, OC43, HKU1 and NL63 (bright green: no amino acid (aa) change, 100% homology; light green: 1 aa difference; yellow: 2 aa difference; orange: 3 aa difference; bright red: 4-10 aa difference, dark red: aa residue at HLA-binding anchor is different, resulting in an IC50 increase by a factor >10 calculated by ANN 4.0; black: no homolog sequence). **c**, Dot plot showing TNF production with and without SARS-CoV-2 peptide re-stimulation after 14-days *in vitro* expansion in a historic control. Bar charts show median with IQR. n=25 historic controls.

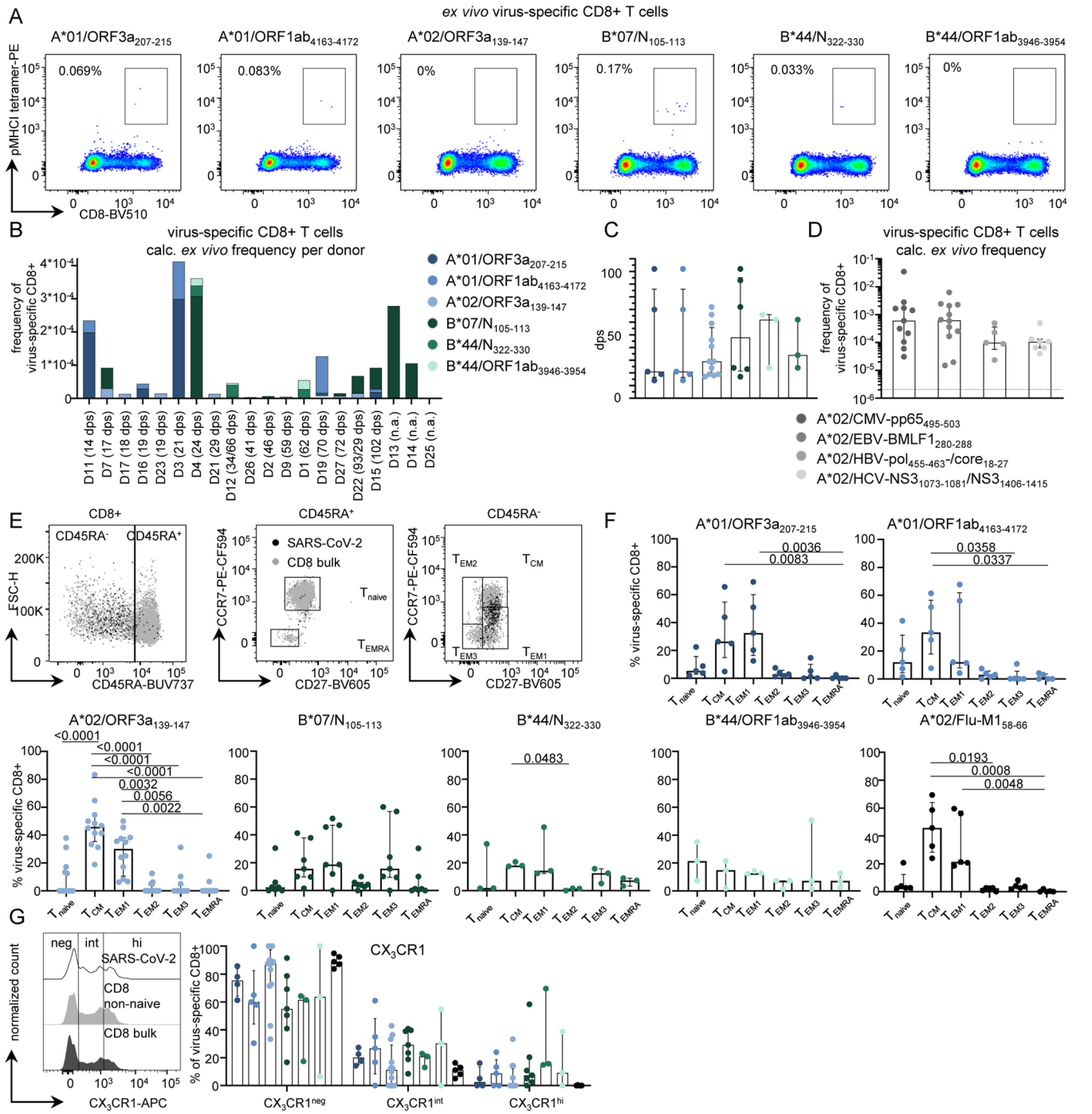

Extended Data Fig. 3 | SARS-CoV-2-specific CD8+ memory T cell subsets. a, Representative dot plots showing A*01/ORF3a$_{207-215}$-, A*01/ORF1ab$_{4163-4172}$-, A*02/ORF3a$_{139-147}$-, B*07/N$_{105-113}$-, B*44/N$_{322-330}$- and B*44/ORF1ab$_{3946-3954}$ -specific CD8+ T cells *ex vivo* after conventional pMHCI tetramer staining (1-2*10^6 PBMCs used). Numbers refer to the respective percentage of pMHCI-tetramer+ cells among CD8+ T cells. **b**, Cumulative depiction of the calculated *ex vivo* frequencies of virus-specific CD8+ T cells for each epitope analyzed in the corresponding donor. **c**, The day post symptom onset (dps) of the respective epitope-specific CD8+ T cells that were analyzed is depicted. **d**, The frequency of A*02/CMV-pp65$_{495-503}$-, A*02/EBV-BMLF1$_{280-288}$-, A*02/HBV-pol$_{455-463}$-/core$_{18-27}$- and A*02/HCV$_{280-288}$-specific CD8+ T cells *ex vivo* after pMHCI tetramer-based enrichment (with 10-20*10^6 PBMCs) was determined. Dashed line indicates detection threshold. **e**, Gating strategy for CD8+ T-cell populations. **f**, Distribution of CD8+ T-cell subsets, naïve T cells (T_{naive}), central memory T cells (T_{CM}), effector memory T cells 1 (T_{EM1}), effector memory T cells 2 (T_{EM2}), effector memory T cells 3 (T_{EM3}) and terminally differentiated effector memory cells re-expressing CD45RA (T_{EMRA}) among CD8+ T cells targeting the different epitopes. **g**, Exemplary histogram showing the gating of cell populations expressing no (neg) CX_3CR1, intermediate (int) CX_3CR1 and high (hi) CX_3CR1 on CD8+ bulk (black) and non-naïve CD8+ T cells (grey) as well as SARS-CoV-2-specific CD8+ T cells (white). % of SARS-CoV-2-specific CD8+ T cells targeting the different epitopes expressing neg, int or hi levels of CX_3CR1. **f**,**g**, *Ex vivo* analyses of virus-specific CD8+ T cells after pMHCI tetramer-based enrichment (10-20*10^6 PBMCs used for enrichment). Bar charts show the median with IQR. n=6 (A*01/ORF3a$_{207-215}$, A*01/ORF1ab$_{4163-417}$), n=12 (A*02/ORF3a$_{139-147}$), n=7 (B*07/N$_{105-113}$), n=3 (B*44/N$_{322-330}$, B*44/ORF1ab$_{3946-3954}$), n=5 (A*02/Flu-M1$_{58-66}$). Statistical significance was assessed by Kruskal-Wallis rank-sum testing including Dunn's multiple comparisons test.

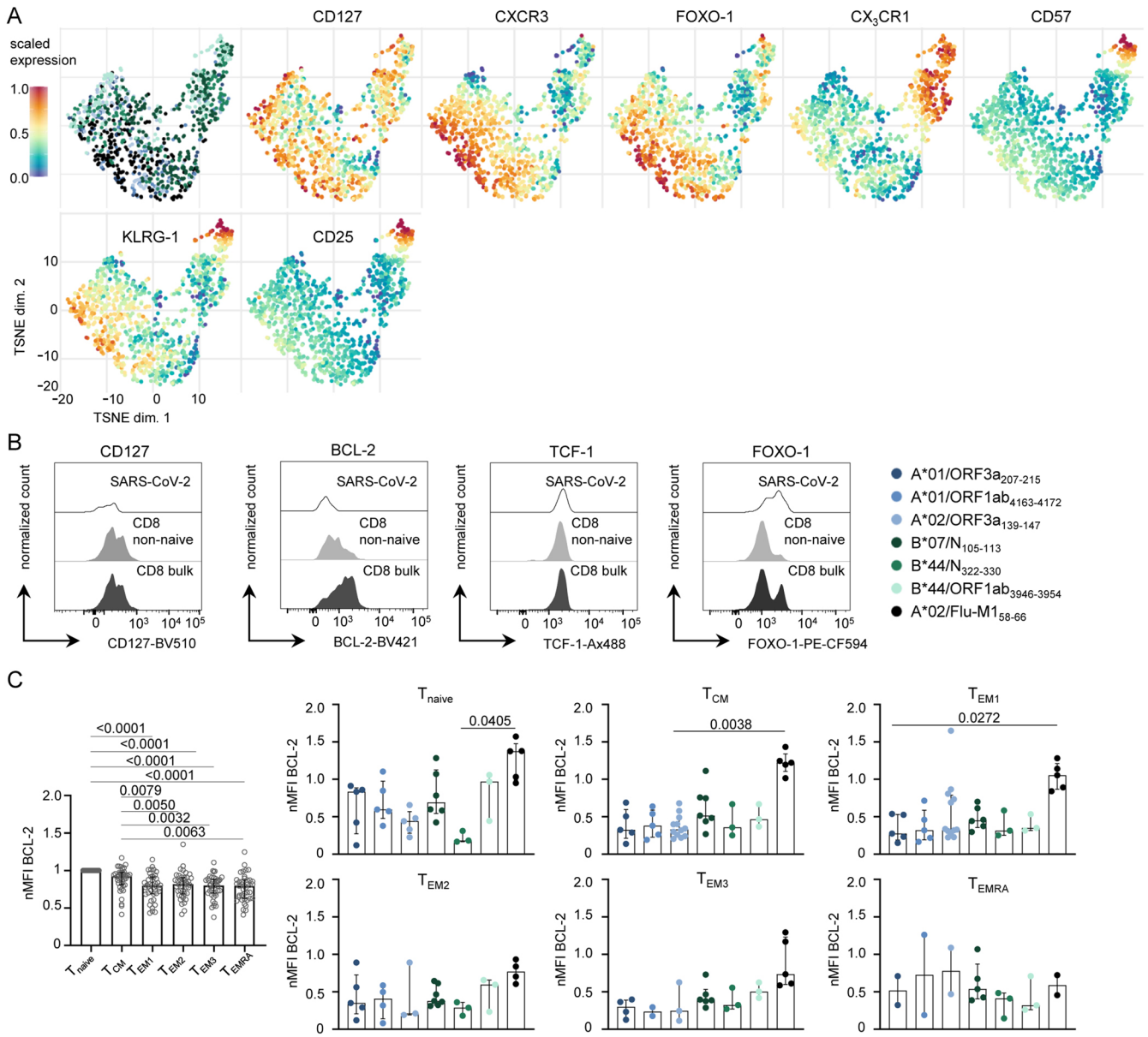

Extended Data Fig. 4 | Phenotype of SARS-CoV-2-specific CD8+ T cells. a, t-SNE representation of flow cytometric data, which were derived from 18 convalescent SARS-CoV-2 individuals after *ex vivo* pMHCI tetramer-based enrichment (10-20*10^6 PBMCs used for enrichment), comparing SARS-CoV-2-specific CD8+ T cells by their HLA restriction (left) and expression levels of CD127, CXCR3, FOXO-1, CX_3CR1, CD57, KLRG-1 and CD25 plotted on the t-SNE plot. **b**, Exemplary histograms depicting the expression levels of CD127, BCL-2, TCF-1 and FOXO-1 on CD8+ bulk (black) and non-naïve CD8+ T cells (grey) as well as SARS-CoV-2-specific CD8+ T cells (white) *ex vivo* after pMHCI tetramer-based enrichment. **c**, BCL-2 expression of different memory cell populations on bulk CD8+ T cells (left) and of SARS-CoV-2- and Flu -specific CD8+ T cells *ex vivo* after pMHCI tetramer-based enrichment of the different CD8+ T-cell subsets. Bar charts show the median with IQR. n=6 (A*01/ORF3$a_{207-215}$, A*01/ORF1$ab_{4163-417}$), n=12 (A*02/ORF3$a_{139-147}$), n=7 (B*07/$N_{105-113}$), n=3 (B*44/$N_{322-330}$, B*44/ORF1$ab_{3946-3954}$), n=5 (A*02/Flu-M1$_{58-66}$). Statistical significance was assessed by Kruskal-Wallis or Friedman rank-sum **C**, testing including Dunn's multiple comparisons test.

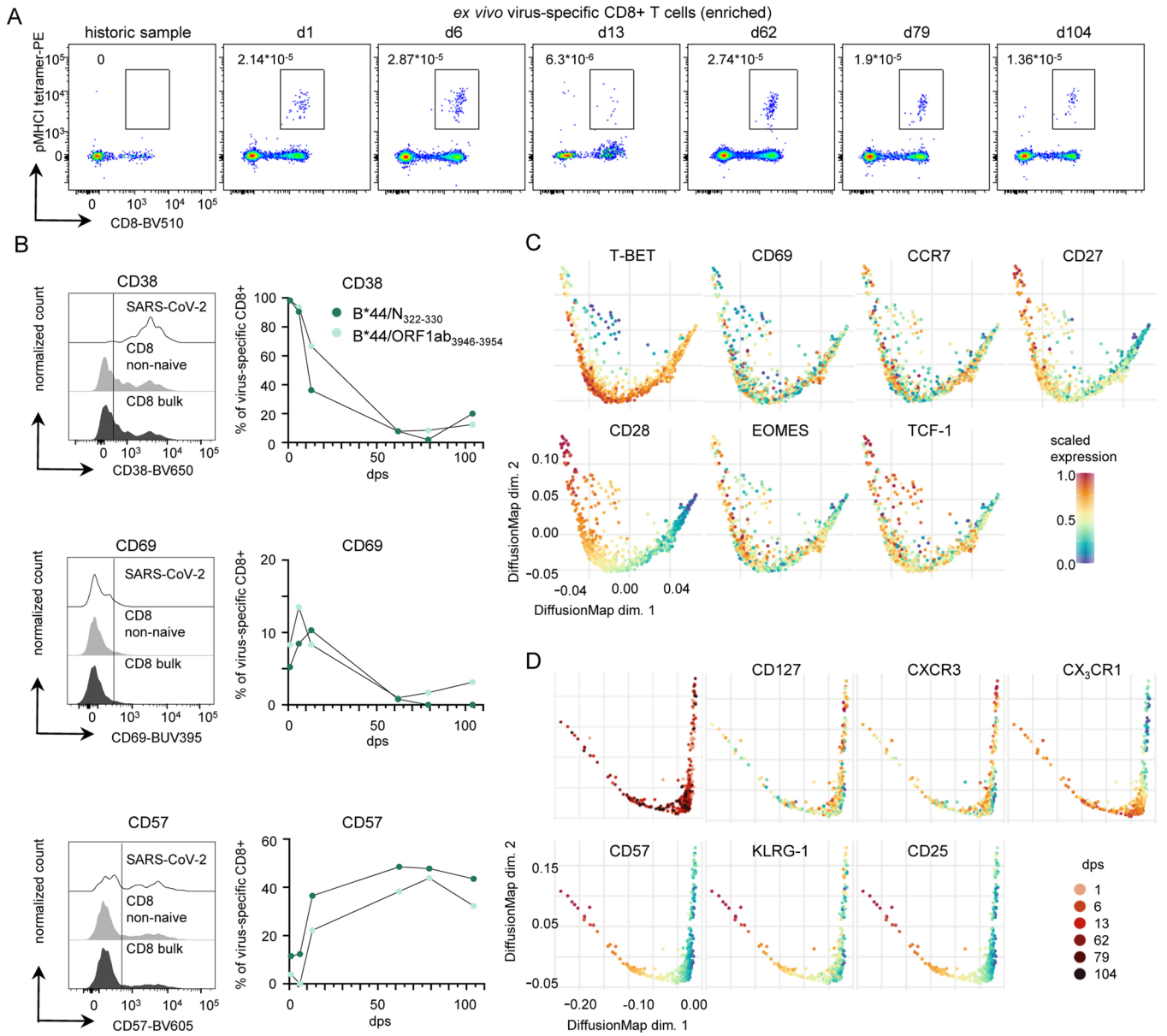

Extended Data Fig. 5 | Longitudinal assessment of the SARS-CoV-2-specific CD8+ T-cell phenotype. a, Dot plots show B*44/ORF1ab$_{3946-3954}$-specific CD8+ T cells *ex vivo* after tetramer-based enrichment (10-20*10^6 PBMCs). Calculated *ex vivo* frequency of virus-specific CD8+ T cells is depicted. **b**, Histograms depicting the protein expression levels on CD8+ bulk (black), CD8+non-naïve (grey) and SARS-CoV-2-specific CD8+ T cells (white) and the expression of these markers on SARS-CoV-2-specific CD8+ T cells at the respective dps. **c**,**d**, Diffusion map of flow cytometric data, derived from longitudinal analysis from D1, showing B*44/N$_{322-330}$- and B*44/ORF1ab$_{3946-3954}$-specific T cells in relation to dps. Protein expression levels (color coded: blue = low expression; red = high expression) are plotted on the diffusion map. Dps are distinguished by a color gradient from light (early time points) to dark red (late time points) color (top left).

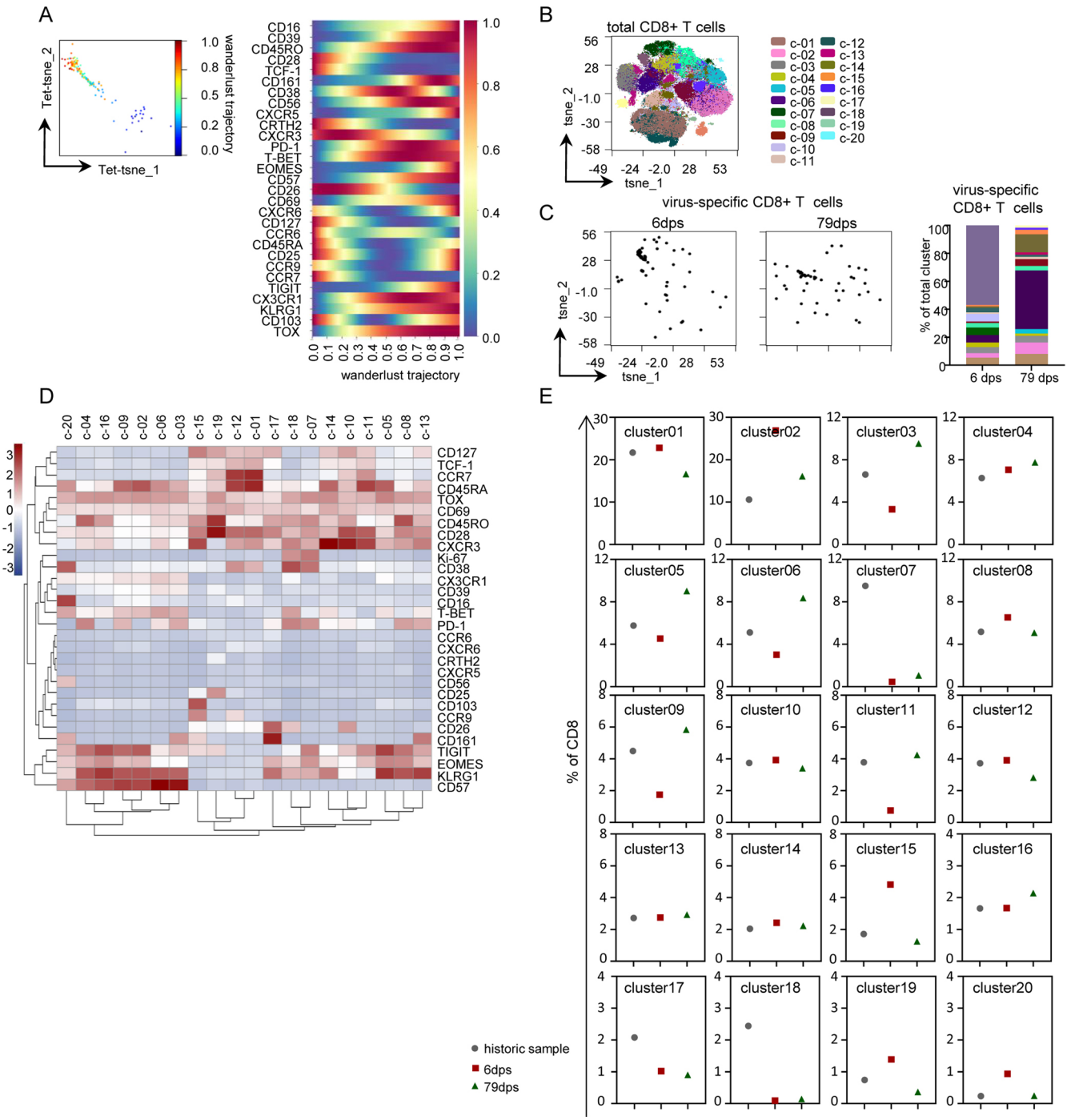

Extended Data Fig. 6 | Deep longitudinal profiling of SARS-CoV-2-specific CD8+ T cells. a, t-SNE map was calculated with all SARS-CoV-2-specific CD8+ T-cell data during (6 dps) and after (79 dps) infection (tet-t-SNE). Wanderlust trajectory analysis was performed on virus-specific CD8+ T cells. Wanderlust trajectory is indicated by heatmap colorization on the tet-t-SNE plot. Marker expression (color-coded: blue, low expression; red, high expression) is depicted according to wanderlust trajectory progression. **b**, The CD8 landscape in cSARS-CoV-2 was calculated using t-SNE on CD8+ T cells from before, during and after infection. Clustering was performed with PARC algorithm and clusters are indicated by the indicated color. **c**, SARS-CoV-2-specific CD8+ T cells are displayed on the t-SNE map. Frequency of virus-specific CD8+ T cells per CD8 cluster is illustrated using stacked bar chart. **d**, Hierarchically clustered heatmap of PARC cluster phenotypes – the indicated marker expression is shown per cluster as z-Score of median signal intensity per channel; blue, low expression; red, high expression. **e**, Frequency of each cluster of historic sample (circle), 6 dps (square) and 79 dps (triangle).

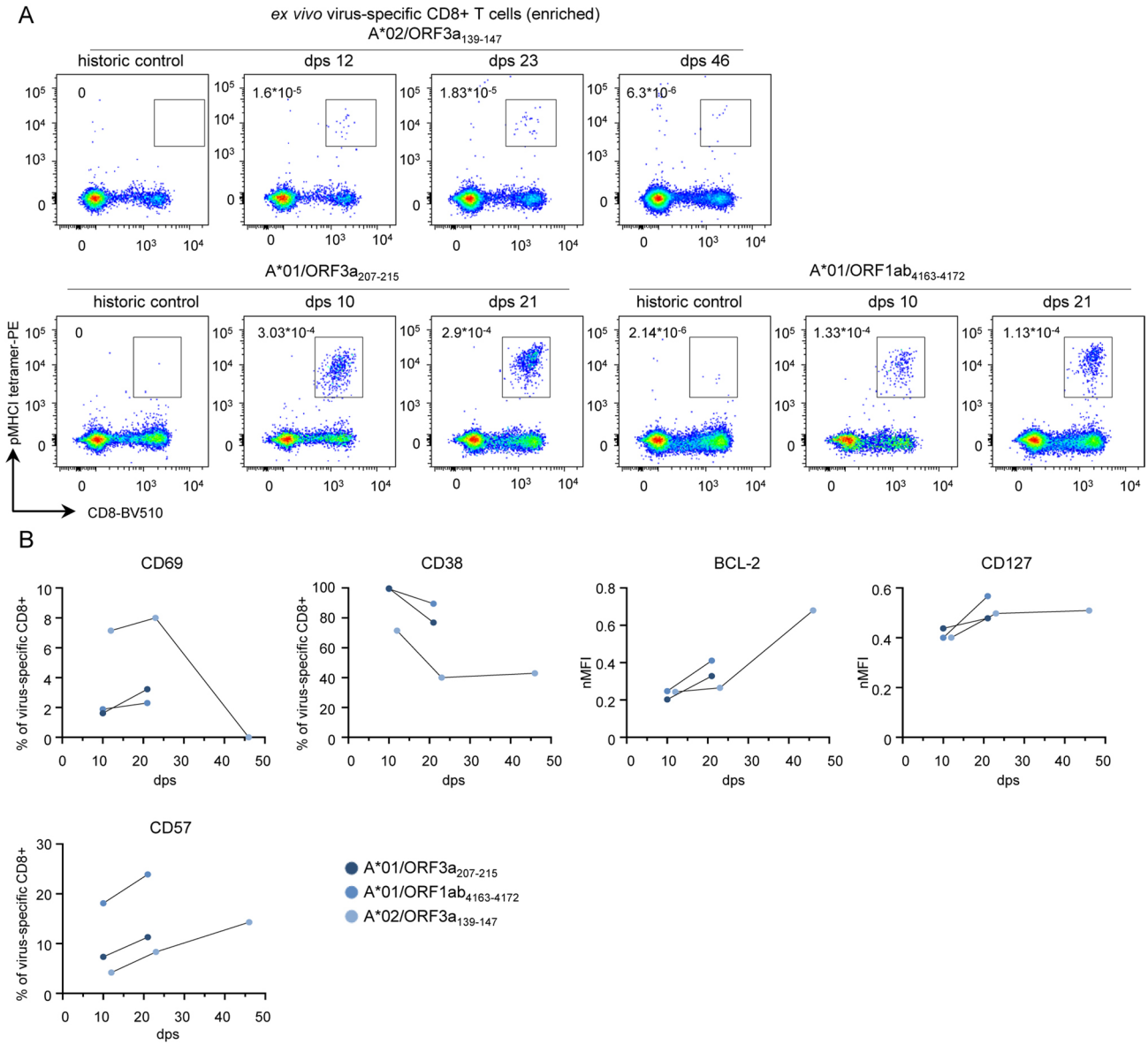

Extended Data Fig. 7 | Additional longitudinal analysis of SARS-CoV-2-specific CD8+ T cells. (a) Representative dot plots showing pMHCI tetramer stainings of A*02/ORF3a$_{139-147}$- (for cSARS-CoV-2 individual D2) and A*01/ORF3a$_{207-215}$-, A*01/ORF1ab$_{4163-4172}$- specific CD8+ T cells (for cSARS-CoV-2 individual D3) *ex vivo* after tetramer-based enrichment (10-20*10^6 PBMCs used for enrichment) at different time points post symptom onset (dps). Numbers refer to the calculated *ex vivo* frequency of virus-specific CD8+ T cells. **(b)** Relative mean fluorescence intensity of proteins expressed on A*02/ORF3a$_{139-147}$- (for cSARS-CoV-2 individual D2) and A*01/ORF3a$_{207-215}$-, A*01/ORF1ab$_{4163-4172}$- specific CD8+ T cells (for cSARS-CoV-2 individual D3) *ex vivo* after tetramer-based enrichment (10-20*10^6 PBMCs used for enrichment) at the respective days post symptom onset (dps).

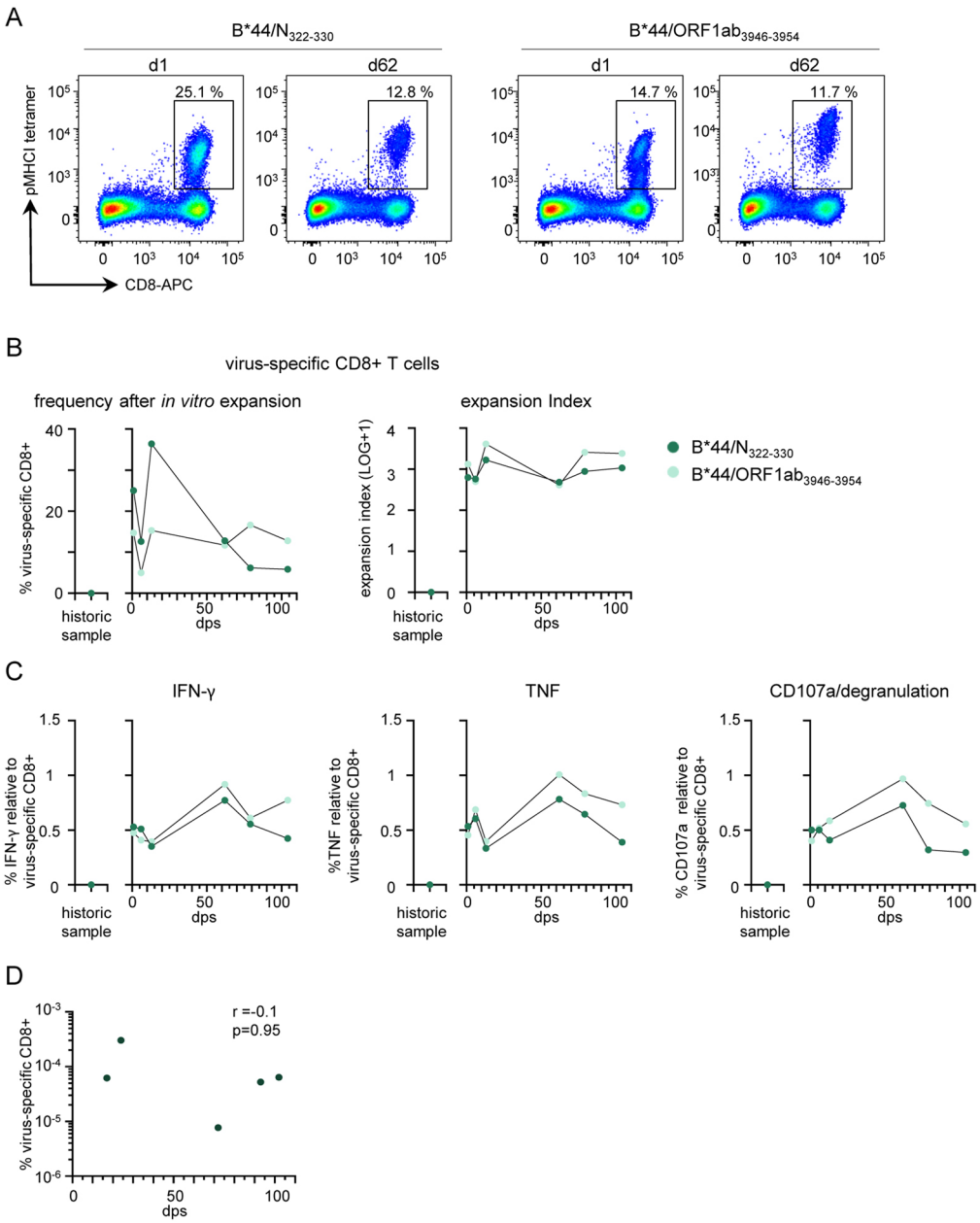

Extended Data Fig. 8 | Longitudinal SARS-CoV-2-specific CD8+ T-cell function. a, Representative dot plots showing pMHCI tetramer stainings of HLA-B*44/$N_{322-330}$ and HLA-B*44/$ORF1ab_{3946-3954}$-specific CD8+ T cells (derived from D1) after 14 days *in vitro* expansion at different time points post symptom onset (dps). Numbers refer to the respective percentage of pMHCI tetramer+ cells out of CD8+ T cells **b**, Frequency and expansion index of virus-specific CD8+ T cells after 14 days *in vitro* expansion at dps. **c**, Expression of IFN-γ, TNF and CD107a/degranulation in percentage relative to the frequency of epitope-specific CD8+ T cells are depicted at dps. **d**, The calculated *ex vivo* frequency of B*07/$N_{105-113}$ -specific CD8+ T cells (10-20*10^6 PBMCs used for enrichment) is indicated at dps. Statistical significance was assessed by Spearman correlation.

nature research

Corresponding author(s): Robert Thimme
Maike Hofmann
Christoph Neumann-Haefelin

Last updated by author(s): Oct 20, 2020

Reporting Summary

Nature Research wishes to improve the reproducibility of the work that we publish. This form provides structure for consistency and transparency in reporting. For further information on Nature Research policies, see our Editorial Policies and the Editorial Policy Checklist.

Statistics

For all statistical analyses, confirm that the following items are present in the figure legend, table legend, main text, or Methods section.

n/a	Confirmed
☐	☒ The exact sample size (*n*) for each experimental group/condition, given as a discrete number and unit of measurement
☐	☒ A statement on whether measurements were taken from distinct samples or whether the same sample was measured repeatedly
☐	☒ The statistical test(s) used AND whether they are one- or two-sided *Only common tests should be described solely by name; describe more complex techniques in the Methods section.*
☐	☒ A description of all covariates tested
☐	☒ A description of any assumptions or corrections, such as tests of normality and adjustment for multiple comparisons
☐	☒ A full description of the statistical parameters including central tendency (e.g. means) or other basic estimates (e.g. regression coefficient) AND variation (e.g. standard deviation) or associated estimates of uncertainty (e.g. confidence intervals)
☐	☒ For null hypothesis testing, the test statistic (e.g. *F*, *t*, *r*) with confidence intervals, effect sizes, degrees of freedom and *P* value noted *Give P values as exact values whenever suitable.*
☐	☒ For Bayesian analysis, information on the choice of priors and Markov chain Monte Carlo settings
☐	☒ For hierarchical and complex designs, identification of the appropriate level for tests and full reporting of outcomes
☐	☒ Estimates of effect sizes (e.g. Cohen's *d*, Pearson's *r*), indicating how they were calculated

Our web collection on statistics for biologists contains articles on many of the points above.

Software and code

Policy information about availability of computer code

Data collection	All software used to perform data collection are described in the methods section of the manuscript or the supportive information. Multiparametric Flow cytometry data was collected by FACSDiva software and CytExpert Software. CyTOF data was collected by CyTOF Helios (Fluidigm)
Data analysis	All codes used to perform bioinformatic analyses are described in the methods section of the manuscript or the supportive information. Multiparametric Flow cytometry data was analyzed using FlowJo software version 10.6.2 (Treestar, Becton Dickinson). The visualization of multiparametric flow cytometry data was done with R version 4.0.2 using the Bioconductor (version: Release (3.11)) CATALYST package (Crowell H, Zanotelli V, Chevrier S, Robinson M (2020). CATALYST: Cytometry dATa anALYSis Tools. R package version 1.12.2, https://github.com/HelenaLC/CATALYST). CyTOF data analysis was performeed by CATALYST: Cytometry dATa anALYSis Tools, R package version 1.12.2, (https://github.com/HelenaLC/CATALYST), and Omiq (Omiq, Inc.). A workflow including dimension reduction using optSNE, PARC clustering analysis and Wanderlust trajectory analysis was implemented in Omiq. Visualization and statistical analysis was performed using GraphPad 8 software. Sequence homology analyses were performed in Geneious Prime 2020.0.3 (https://www.geneious.com/) using Clustal Omega 1.2.2 alignment with default settings.

For manuscripts utilizing custom algorithms or software that are central to the research but not yet described in published literature, software must be made available to editors and reviewers. We strongly encourage code deposition in a community repository (e.g. GitHub). See the Nature Research guidelines for submitting code & software for further information.

Data

Policy information about availability of data

All manuscripts must include a data availability statement. This statement should provide the following information, where applicable:

- Accession codes, unique identifiers, or web links for publicly available datasets
- A list of figures that have associated raw data
- A description of any restrictions on data availability

Raw data in this study are provided in the Supplementary Dataset, at https://github.com/sagar161286/SARSCoV2_specific_CD8_Tcells (flow cytometry data) and at https://flowrepository.org/experiments/3159 (mass cytometry data). Additional supporting data are available from the corresponding authors upon reasonable request. All requests for raw and analyzed data and materials will be reviewed by the corresponding authors to verify if the request is subject to any intellectual property or confidentiality obligations. Patient-related data not included in the paper were generated as part of clinical examination and may be subject to patient confidentiality. Any data and materials that can be shared will be released via a Material Transfer Agreement. Source data are provided with this paper.
Reference viral sequences (SARS-CoV-2 (MN908947.3) https://www.ncbi.nlm.nih.gov/nuccore/MN908947, 229E (NC_002645) https://www.ncbi.nlm.nih.gov/nuccore/NC_002645, HKU1 (NC_006577) https://www.ncbi.nlm.nih.gov/nuccore/NC_006577, NL63 (NC_005831)https://www.ncbi.nlm.nih.gov/nuccore/NC_005831, OC43 (NC_006213)https://www.ncbi.nlm.nih.gov/nuccore/NC_006213, MERS (NC_019843)https://www.ncbi.nlm.nih.gov/nuccore/NC_019843, SARS-CoV-1 (NC_004718)https://www.ncbi.nlm.nih.gov/nuccore/NC_004718) were downloaded from the NCBI database (https://www.ncbi.nlm.nih.gov/). In silico peptide binding was analyzed with ANN 4.0 on the Immune Epitope Database website (https://www.iedb.org/).
Code availability: R code to reproduce the analysis of multiparametric flow-cytometry data is available at https://github.com/sagar161286/SARSCoV2_specific_CD8_Tcells. Detailed settings for dimension reduction, clustering and trajectory analysis of mass cytometry data is available via the platform Omiq.ai upon reasonable request.

Field-specific reporting

Please select the one below that is the best fit for your research. If you are not sure, read the appropriate sections before making your selection.

☒ Life sciences ☐ Behavioural & social sciences ☐ Ecological, evolutionary & environmental sciences

For a reference copy of the document with all sections, see nature.com/documents/nr-reporting-summary-flat.pdf

Life sciences study design

All studies must disclose on these points even when the disclosure is negative.

Sample size	Patients were recruited and patient material was banked at the University Hospital Freiburg; inclusion criteria were: (1) 25 COVID-19 convalescent individuals following a mild course of SARS-CoV-2 infection, SARS-CoV-2 infection was confirmed by positive PCR testing from oropharyngeal swab and/or SARS-CoV-2 spike IgG positive antibody testing, (2) 31 age and sex-matched historic controls and (3) 3 longitudinal cases (historic, acute, convalescent). These numbers are comparable to many other studies in the research field of human immunology and proved to be sufficient for the generation of reproducible results.
Data exclusions	For flow cytometrical analysis, cell populations containing less than 5 cells were excluded. This data exclusion strategy has been applied and validated previously by our group to gain reproducible results in studies investigating virus-specific CD8+ T cells in human viral infections.
Replication	Analyses were performed in independent experiments. Findings were reproducible. Independent experiments: flow cytometry analysis: 6 (A*01/ORF3a207-215, A*01/ORF1ab4163-417), 12 (A*02/ORF3a139-147), 7 (B*07/N105-113), 3 (B*44/N322-330, B*44/ORF1ab3946-3954) and 5 (A*02/Flu-M158-66) independent experiments (Figure 2, Figure 4B-C, Extended Data Figure 3, Extended Data Figure 4), 4 experimental days (Figure 3, Extended Data Figure 5, Extended Data Figure 6, Extended Data Figure 7, Extended Data Figure 8), 7 (cSARS-CoV-2) and 5 (D-E) or 3 (F)(historic controls) independent experiments (Figure 4D-F),
Randomization	Convalescent SARS-CoV-2 donors were selected based on availability and HLA-typing. The covariates age and gender are well-documented: Median age of convalescent individuals was 34,3 years, of historic controls 36,9 years and of longitudinal cases 42,7. The gender ratio of convalescent individuals was m/f: 11/14, of historic controls m/f: 8/21 (2 not available) and of longitudinal cases m/f: 2/1.
Blinding	Blinding was not applied. Non-objective parameters were not included in the study design. Due to standardized analyses of the flow cytometric data set, biased analysis can be excluded.

Reporting for specific materials, systems and methods

We require information from authors about some types of materials, experimental systems and methods used in many studies. Here, indicate whether each material, system or method listed is relevant to your study. If you are not sure if a list item applies to your research, read the appropriate section before selecting a response.

Materials & experimental systems

n/a	Involved in the study
☐	☒ Antibodies
☒	☐ Eukaryotic cell lines
☒	☐ Palaeontology and archaeology
☒	☐ Animals and other organisms
☐	☒ Human research participants
☒	☐ Clinical data
☒	☐ Dual use research of concern

Methods

n/a	Involved in the study
☒	☐ ChIP-seq
☐	☒ Flow cytometry
☒	☐ MRI-based neuroimaging

Antibodies

Antibodies used

Flow Cytometry:
BD Biosciences
anti-CCR7-PE-CF594 (150503, 1:50) Cat# 353232
anti-CCR7-BUV395 (3D12, 1:50) Cat# 740267
anti-CCR7-BV421 (150503, 1:33) Cat# 562555
anti-CD4-BV786 (L200, 1:200) Cat# 563914
anti-CD8-BUV496 (SK1, 1:100) Cat# 564804
anti-CD8-BUV510 (SK1, 1:100) Cat# 563919
anti-CD8-APC (SK-1, 1:200) Cat# 345775
anti-CD27-BV605 (L128, 1:200) Cat# 562655
anti-CD28-BV421 (CD28.2, 1:100) Cat# 302930
anti-CD28-BV711 (CD28.2, 1:100) Cat# 563131
anti-CD45RA-BV786 (HI100, 1:800) Cat# 304139
anti-CD45RA-BUV737 (HI100, 1:200) Cat# 564442
anti-CD69-BUV395 (FN50, 1:50) Cat# 564364
anti-CD107a-APC (H4A3, 1:100) Cat# 560664
anti-CD127-BV510 (HIL-7R-M21, 1:25) Cat# 563086
anti-IFN-γ-FITC (25723.11, 1:8) Cat# 340449
anti-IL-21-PE (3A3-N2.1, 1:25) Cat# 560463
anti-PD-1-BV786 (EH12.1, 1:33) Cat# 563789
anti-TNF-PE-Cy7 (Mab11, 1:400) Cat# 557647
anti-BCL-2-BV421 (100, 1:200) Cat# 658709
ViaProbe (7-AAD, 1:33) Cat# 555816

Biolegend
anti-CD25-BV650 (BC96, 1:33) Cat# 302633
anti-CD38-BV650 (HB-7, 1:400) Cat# 356620
anti-CD57-BV605 (QA17A04, 1:100) Cat# 563895
anti-CX3CR1-APC (2A9-1, 1:50) Cat# 341610
anti-CXCR3-PerCP-Cy5.5 (G025H7, 1:33) Cat# 353714
anti-IL-2-PerCP-Cy5.5 (MQ1-17H12, 1:100) Cat# 500322
anti-IL17A-BV605 (BL168, 1:100) Cat# 512326
anti-PD-1-PE-Cy7 (EH12.2H7, 1:200) Cat#1 329918
anti-rabbit-PE-CF594 (Poly4064, 1:200) Cat# 406418
anti-CD45RA-BV510 (HI100, 1:200) Cat# 304142

Cell Signalling
anti-FOXO1-pure (C29H4, 1:33) Cat# 2880
anti-TCF1-AlexaFluor488 (C63D9, 1:100) Cat# 6444

eBioscience
anti-EOMES-PerCP-eF710 (WD1928, 1:50) Cat# 46-4877
anti-CD14-APC-eFluor780 (61D3, 1:400) Cat# 47-0149-42
anti-CD19-APC-eFluor780 (HIB19, 1:400) Cat# 47-0199
anti-CD27-FITC (0323, 1:100) Cat# 11-0279
anti-T-BET-PE-Cy7 (4B10, 1:200) Cat# 25-5825
anti-KLRG1-BV711 (13F12F2, 1:50) Cat# 67-9488-42
Viability Dye (APC-eFluor780 1:200, 1:400) Cat# 65-0865
anti-TOX-eFluor660 (TRX10, 1:100) Cat# 50-6502

Mass Cytometry:
Fluidigm
anti-CD45-89Y (HI30 1:100) Cat#3089003B
anti-CCR6-141Pr (G034E3 1:200) Cat#3141003A
anti-CD69-144Nd (FN50 1:100) Cat#3144018B
anti-CD25-149Sm (2A3 1:400) Cat#3149010B
anti-CD21-152Sm (BL13 1:400) Cat#3152010B
anti-TCR Vα7.2-153Eu (3C10 1:400) Cat#3153024B

anti-CXCR3-156Gd (G025H7 1:400) Cat#3156004B
anti-CCR7-159Tb (G043H7 1:100) Cat#3159003A
anti-T-bet-160Gd (4B10 1:800) Cat#3160010B
anti-FoxP3-162Dy (PCH1011:800) Cat#3162011A
anti-CD161-164Dy (HP3G10 1:100) Cat#3164009B
anti-CCR4-175Lu (L291H4 1:100) Cat#3175035A
anti-CD16-209Bi (3G8 1:400) Cat#3209002B
Anti-APC-176Yb (APC003 1:100) Cat#3176007B

eBioscience
anti-KLRG1 (13F12F2 1:400) Cat# 16-9488-85 in house conjugation with 173Yb

BD Biosciences
anti-Ki-67 pure (B56 1:200) Cat#556003 in house conjugation with 146Nd
anti-CXCR5 (RF8B2 1:200) Cat#552032 in house conjugation with 170Er

Biolegend
anti-CD4 (RPA-T4 1:200) Cat#300502 in house conjugation with 111Cd
anti-CD3 (UCHT1 1:400) Cat#300402 in house conjugation with 112Cd
anti-CD39 (A1 1:50) Cat#328202 in house conjugation with 113In
anti-CD45RO (UCHL1 1:50) Cat#304239 in house conjugation with 114Cd
anti-CD8 (RPA-T8 1:400) Cat#301002 in house conjugation with 116Cd
anti-CD26 (BA5b 1:400) Cat#302702 in house conjugation with 142Nd
anti-Nkp46 (9E2 1:800) Cat#331902 in house conjugation with 143Nd
anti-CD19 (HIB19 1:400) Cat#302202 in house conjugation with 145Nd
anti-CD45RA (H100 1:200) Cat#304143 in house conjugation with 147Sm
anti-CXCR6 (K041E5 1:100) Cat#356002 in house conjugation with 148Nd
anti-CD127 (HIL-7R-M21 1:100) Cat#351302 in house conjugation with 150Nd
anti-CCR9 (L053E8 1:100) Cat#358902 in house conjugation with 154Sm
anti-CRTH2 (BM16 1:100) Cat#350102 in house conjugation with 155Gd
anti-PD-1 (EH12.2H7 1:100) Cat#329902 in house conjugation with 158Gd
anti-CD28 (CD28.2 1:200) Cat#302902 in house conjugation with 161Dy
anti-TCF-1 (C398.4A 1:200) Cat#655202 in house conjugation with 163Dy
anti-CD56 (NCAM16.2 1:400) Cat#318302 in house conjugation with 168Er
anti-CX3CR1 (K0124E1 1:400) Cat#355702 in house conjugation with 172Yb
anti-CD103 (Ber-ACT8 1:800) Cat#350202 in house conjugation with 174Yb
anti-PE (PE001 1:100) Cat#408102 in house conjugation with 151Eu

Invitrogen
anti-CD57 (TB01 1:800) Cat#16-0577-85 in house conjugation with 115In
anti-EOMES (WD1928 1:200) Cat#14-4877-82 in house conjugation with 165Ho
anti-CD38 (HIT2 1:200) Cat#14-0389-82 in house conjugation with 167Er
anti-TIGIT (MBSA43 1:100) Cat#16-9500-82 in house conjugation with 169Tm
anti-TCRγδ (B1 1:50) Cat#TCR1061 in house conjugation with 171Yb

Milteny
TOX- APC (REA473 1:50) Cat#130-118-335

Validation

standardized analysis in different cohorts, antibody titration on PBMCs including unstained controls, comparisons of different antibody clones and conjugates and validated by publications:
CCR7, clone 3D12 and 150503: antibody titration on PBMCs; control clone G043H7; validated with respect to differential expression of naïve and non-naïve T cell subpopulations
CD4, clone L200: antibody titration on PBMCs; control clones SK3; using B cells as negative control
CD8, clone SK1: antibody titration on PBMCs; control clones GHI/75 and RPA-T8; using B cells as negative control
CD27, clone L128: antibody titration on PBMCs; control clone O323; validated with respect to differential expression of naïve and non-naïve T cell subpopulations
CD28,clone CD28.2: antibody titration on PBMCs; control clone B-T3; validated with respect to differential expression of naïve and non-naïve T cell subpopulations
CD45RA, clone HI100: antibody titration on PBMCs; validated with respect to differential expression of naïve and non-naïve T cell subpopulations
CD69, clone FN50: antibody titration on PBMCs; validated with respect to differential expression of activated and non-activated T cell subpopulations
CD107a, clone H4A3: antibody titration on PBMCs; validated with respect to differential expression of activated and non-activated T cell subpopulations
CD127 , clone HIL-7R-M21: antibody titration on PBMCs; control clone A019D5; validated with respect to differential expression of naïve and non-naïve T cell subpopulations
IFNɣ, clone 25723.11: antibody titration on PBMCs; control clone 4S.B3; validated with respect to differential expression of activated and non-activated T cell subpopulations
IL-21, clone 3A3-N2.1: antibody titration on PBMCs; validated with respect to differential expression of activated and non-activated T cell subpopulations
PD-1, clone EH12.2H7 and EH12.1: antibody titration on PBMCs; control clones eBioJ105; validated with respect to differential expression of naïve and non-naïve T cell subpopulations
TNF, clone MAb11: antibody titration on PBMCs; validated with respect to differential expression of activated and non-activated T cell subpopulations
Bcl-2 , clone 100: antibody titration on PBMCs; validated with respect to differential expression of naïve and non-naïve T cell

subpopulations
CD25, clone BC96: antibody titration on PBMCs; control clone M-A251; validated with respect to differential expression of activated and non-activated T cell subpopulations
CD38, clone HB7: antibody titration on PBMCs; control clone HIT2; validated with respect to differential expression of naïve and non-naïve T cell subpopulations
CD57, clone QA17A04: antibody titration on PBMCs; control clone NK-1; validated with respect to differential expression of naïve and non-naïve T cell subpopulations
CX3CR1, clone 2A9-1: antibody titration on PBMCs; validated with respect to differential expression of naïve and non-naïve T cell subpopulations
CXCR3, clone G025H7: antibody titration on PBMCs; control clone 1C6/CXCR3; validated with respect to differential expression of activated and non-activated T cell subpopulations
IL-2, clone MQ1-17H12: antibody titration on PBMCs; validated with respect to differential expression of activated and non-activated T cell subpopulations
IL-17A, clone BL168: antibody titration on PBMCs; control clone eBio64DEC17; validated with respect to differential expression of activated and non-activated T cell subpopulations
anti-rabbit-PE-CF594, clone Poly4064: antibody titration on PBMCs; validated with respect to differential expression of cells stained with primary Rabbit IgG and primary Mouse IgG1.
FOXO1, clone C29H4: antibody titration on PBMCs; validated with respect to differential expression of naïve and non-naïve T cell subpopulations
TCF-1, clone C63D9: antibody titration on PBMCs; control clone 7F11A10; validated with respect to differential expression of naïve and non-naïve T cell subpopulations
Eomes, clone WD1928: antibody titration on PBMCs; validated with respect to differential expression of naïve and non-naïve T cell subpopulations
CD14 , clone 61D3: antibody titration on PBMCs; control clones M5E2 and MϕP9; using T cell populations as negative control
CD19, clone HIB19: antibody titration on PBMCs; control clone SJ25C1; using T cell populations as negative control
T-bet, clone 4B10: antibody titration on PBMCs; control clones O4-46; validated with respect to differential expression of naïve and non-naïve T cell subpopulations
KLRG1, clone 13F12F2: antibody titration on PBMCs; validated with respect to differential expression of naïve and non-naïve T cell subpopulations
TOX1, clone TRX10: antibody titration on PBMCs; control clone REA473; validated with respect to differential expression of naïve and non-naïve T cell subpopulations

The antibody clones used for mass cytometry were validated in flow and mass cytometry experiments. Titration and Validation experiments for mass cytometry antibodies after conjugation were performed on PBMCs from healthy individuals. Gated lymphocyte populations expressing a given marker were used as positive control.

Human research participants

Policy information about studies involving human research participants

Population characteristics	25 convalescent patients with mild SARS-CoV-2 infection (cross-sectional), carrying either of the following HLA alleles: HLA-A*01:01, -A*02:01, -A*03:01, -A*11:01, -A*24:02, -B*07:02, -B*08:01, -B*15:01, -B*40:01, -B*44:02/03, 31 age- and sex-matched historic controls (cross-sectional) and 3 longitudinal cases (historic, acute, convalescent) were recruited at the University Hospital Freiburg. Median age of convalescent individuals was 34,3 years, of historic controls 36,9 years and of longitudinal cases 42,7. The gender ratio of convalescent individuals was m/f: 11/14, of historic controls m/f: 8/21 (2 not available) and of longitudinal cases m/f: 2/1.
Recruitment	SARS-CoV-2-infected and SARS-CoV-2-convalescent patients were recruited at the University Hospital Freiburg, samples were banked and retrospectively selected according to the following inclusion criteria: HLA-A*01:01, -A*02:01, -A*03:01, -A*11:01, -A*24:02, -B*07:02, -B*08:01, -B*15:01, -B*40:01, -B*44:02/03. Banked samples from sex-, age- and HLA-matched historic controls were retrospectively selected.
Ethics oversight	Written informed consent was obtained from all participants and the study was conducted according to federal guidelines, local ethics committee regulations (Albert-Ludwigs-Universität, Freiburg, Germany; vote #: 322/20) and the Declaration of Helsinki (1975).

Note that full information on the approval of the study protocol must also be provided in the manuscript.

Flow Cytometry

Plots

Confirm that:

☒ The axis labels state the marker and fluorochrome used (e.g. CD4-FITC).

☒ The axis scales are clearly visible. Include numbers along axes only for bottom left plot of group (a 'group' is an analysis of identical markers).

☒ All plots are contour plots with outliers or pseudocolor plots.

☒ A numerical value for number of cells or percentage (with statistics) is provided.

Methodology

Sample preparation	Cryopreserved isolated human PBMCs were thawed and prepared for flow cytometry or in vitro expansion described in the methods section
Instrument	FACSCanto II, LSRFortessa (BD, Germany) or CytoFLEX (Beckman Coulter), CyTOF Helios (Fluidigm),
Software	FlowJo_v10.6.2 (Treestar), R version 4.0.2 using the Bioconductor (version: Release (3.11)) . CATALYST: Cytometry dATa anALYSis Tools. R package version 1.12.2, https://github.com/HelenaLC/CATALYST), Omiq (Omiq, Inc.)
Cell population abundance	Abundance of SARS-CoV-2-specific CD8+ T cells are low (<10^-4 %)
Gating strategy	Lymphocytes gated on FSC-A and SSC-A, Doublet exclusion on FSC-A and FSC-H and FSC-A and FSC-W, Exclusion of dead cells, B cells and monocytes, Gating on CD8+ cells, Exclusion of naive cells (CCR7+CD45RA+), Gating of SARS-CoV-2-specific CD8+ T cells via tetramers described in methods part.

☒ Tick this box to confirm that a figure exemplifying the gating strategy is provided in the Supplementary Information.